

國立臺灣大學理學院物理學系

博士論文

Department of Physics

College of Science

National Taiwan University

Doctoral Dissertation



電磁波於二聚體間激發的極化電荷強化現象  
和微波燒結中的非熱效應

Electromagnetic-Wave-Induced Polarization Charge  
Enhancement in Dimer Interactions and a Non-Thermal  
Effect in Microwave Sintering

劉立中

Li-Chung Liu

指導教授：朱國瑞 博士

Advisor: Kwo Ray Chu, Ph.D.

中華民國 112 年 1 月

January 2023

國立臺灣大學博士學位論文

口試委員會審定書

電磁波於二聚體間激發的極化電荷強化現象和微波燒結中的非熱效應

Electromagnetic-Wave-Induced Polarization Charge Enhancement in Dimer

Interactions and a Non-thermal Effect in Microwave Sintering

本論文係 劉立中 君 (學號 F06222048) 在國立臺灣大學理學院物理學系所完

成之博士學位論文，於民國 112 年 1 月 5 日承

下列考試委員審查通過及口試及格，特此證明

口試委員： 朱國瑞 (簽名)

(指導教授)

陳仕君

姜唯元

張存續

陳漢穎

鄭復興

系主任：  (簽名)

## 誌謝

在應用電磁實驗室的這五年半間，感謝朱國瑞院士對我的細心指導，使我從一開始對研究一知半解，到如今能完成一點小小的成果。朱老師對研究的熱情也深深影響了我，這些年來經常受到老師對物理研究的啟發與對人生的教導。期許自己有一天也能將研究作為人生志向，兢兢業業一甲子。

在這段研究旅途中，有幸獲得許多優秀學長姊的提攜與引領。感謝陳漢穎學長，提供宏碩系統的實習機會，讓我接觸微波物理在工業界的運用；感謝陳仕宏學長，當我在數值分析與模擬遇到瓶頸時給予指引；感謝鄭復興學長，讓我有參與在國防部計畫中學習；感謝張存續學長，激發我很多微波在應用科學上的方向；感謝姜惟元學長，和我分享研究想法和職涯規劃；感謝鄧亘皓學長，手把手教會我許多實驗操作和模擬撰寫；感謝蔡有方學長，在實驗和研究困境中給予我協助與支持；謝謝林明勳學弟，讓我明白獨立研究的重要性。

Many thanks to Dr. Larry Barnett for the design and construction of apparatus in our laboratory. It is my fortune and honor to learn from him.

在台大的十年求學路，亦陪伴著諸多良師的照顧。感謝熊怡老師、裴思達老師、王偉華老師、汪治平老師、王遠義老師、曾詣涵老師、張顏暉老師、侯維恕老師、林清涼老師、柯俊成老師和莊國禎教練。是你們的鼓勵與支持，讓我選擇走向物理這條路，也是我不斷克服挫折，繼續向前的動力。

最後，感謝家人與朋友對我一路以來的支持。

劉立中 2022 年 12 月 31 日，於物理館 103 室

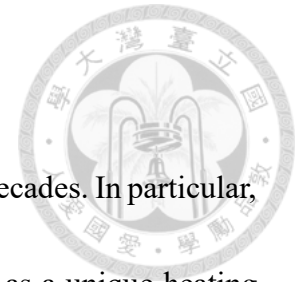
## 摘要

介電質的微波特性多年來一直被廣泛研究，工業上也有相當多的應用。尤其是微波對介電質加熱所具備的非接觸性、高均勻度、高加熱速率等優點，使其在多個領域大放異彩：化學分析、食物製程、害蟲控制、空氣淨化等，皆有大量的論文研究，探討其適用的範圍。然而，許多重要的微波加熱介電質物理卻鮮少有人討論，像是極化電荷屏蔽效應、二聚體的電場相互增強、微波共振與多個物理效應之間的競爭關係。本篇論文將以數學解析解、電磁模擬與實驗結果交叉論證，用簡單的物理模型解釋上述現象。

首先，我將對介電質在微波照射下的物理做簡單介紹，幫助讀者在後續文章中理解；其次，以數學解析解分析均勻靜電場中與平面波照射下的介電質圓球，分別了解極化電荷屏蔽效應和微波共振，並以準靜態近似將兩種現象在不同大小尺度下的介電質做銜接；接著，介紹二聚體的電場相互強化，以兩個不同頻率微波（無磁場的低頻段 27 MHz 和強烈微波共振的高頻段 2.45 GHz）的電磁模擬與實驗結果，展示其強化效果的適用性；最後，將上述的三種現象帶入到介電質材料的微波燒結中，以電磁模擬與簡單物理模型解釋在目前燒結中的非熱效應，如微波燒結溫度較傳統方式低溫、燒結後材料結構改變等。

關鍵字：介電質微波加熱、極化電荷屏蔽效應、微波共振、準靜態、電場相互強化、電磁波放電現象、介電質材料燒結

## ABSTRACT

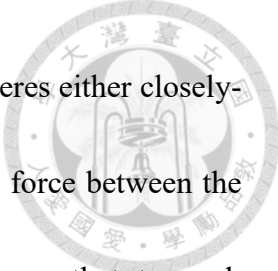


Microwave phenomena in dielectrics have been researched for decades. In particular, microwave is extensively used in industrial applications, especially as a unique heating source. The advantages of microwave heating include its non-contact nature, great penetration depth, and high heating rate, as compared to the conventional methods. These advantages lead to numerous, multi-disciplinary research activities in, for example, chemical synthesis, plasma generation, food processing, pest control, and cultural heritage preservation. However, there are also a large number of problems, notably heating non-uniformity, which have hindered further advances of this method. Some of these problems are obvious (such as standing wave pattern in a resonator), some have been understood (such as thermal runaways), and some are physics issue which have not yet been realized or fully understood (such as the occurrence of sparks and the non-thermal effects in some applications). This dissertation addresses a few of such issues, all originating from the induced polarization charges and some complicated by electromagnetic resonances in the heated body. Based on a dimer model, analytic theories, electromagnetic simulations, and experiments are carried out for the understanding of polarization-charge shielding/enhancement of the applied electric field and a potential non-thermal effect due to the attractive force between polarization charges.



We begin with a review of relevant basic theory on DC and AC field interactions with a dielectric object. Analytic expressions are presented to demonstrate two important microwave effects of dielectric spheres: the polarization charge shielding effect in a static, uniform, external electric field and the internal microwave resonance induced by a plane wave.

Next, we consider a decades-long, popular-science puzzle in the form of sparks ignited by the electromagnetic wave in the gap of two grapes in a household microwave oven. The latest and generally-accepted physical explanation models the two grapes by two water spheres (referred to as a dimer). It attributes the sparks to the merging of electromagnetic resonances from each sphere of the dimer into a hot spot. We point out the flaws of the “electromagnetic origin” of the hot spot, then propose a new explanation of electric nature. The electric field in the gap of the dimer due to mutual enhancement of the induced polarization charges on the gap surfaces is shown in simulation to be high enough to cause an air breakdown, hence the sparks. This electric origin is verified in experiments in two ways. First, the sparks are shown to occur at 27 MHz, at which no electromagnetic resonance in the dimer is possible. Second, the electromagnetic origin would result in a repulsive force between the two spheres, while the electric origin would lead to an attractive force. Our experiment at 2.45 GHz clearly demonstrates the attractive motion of the two spheres.



The validation of a strong gap electric field between the two spheres either closely-spaced or in contact suggests the existence of a significant attractive force between the two spheres. On the other hand, in microwave sintering, it is well known that, to reach the same degree of density, the required temperature is well below that in a conventional oven. Reasons for this advantage are still under investigation although several theories have been proposed. We thus end the dissertation with a rigorous analytical analysis to put the attractive force in closed form. The evaluation of the forces under common sintering conditions yields rather large values to allow us to propose a new non-thermal mechanism for the interpretation of the lower temperature in microwave sintering. This mechanism explains an early microwave sintering experiment, while further experimental evidences are needed to assess its significance in a more conclusive manner.

Keywords: Dielectric microwave heating; Polarization charge shielding effect; Microwave resonance; Quasi-static regime; Gap electric field intensification; Electromagnetic wave ignited sparks; Dielectric material sintering

# CONTENTS



口試委員會審定書	
誌謝	i i
摘要	iii
Abstract	iv
Contents	vii
<b>Chapter 1 Review of Relevant Microwave Physics</b>	<b>1</b>
1.1 Microwave Heating of Dielectric Materials	1
1.2 Penetration Depth	5
1.3 Shielding Effect in a Uniform Static Electric Field	6
1.4 Microwave Resonance in Dielectric Materials	8
1.5 Quasi-static Regime	10
<b>Chapter 2 Microwave Phenomena in Dielectrics</b>	<b>12</b>
2.1 A Dielectric Sphere in a Uniform Static Electric Field	12
2.2 A Dielectric Sphere Irradiated by a Plane Wave	15
2.3 Microwave properties of a Water Sphere	19
<b>Chapter 3 On Electromagnetic Wave Ignited Sparks in Aqueous Dimers</b>	<b>24</b>
3.1 Theory and Experiment at Low Microwave Frequency	25
3.2 Validity Range of the Quasi-static Regime	31



3.3	Theory and Experiment at High Microwave Frequency	35
3.4	Microwave-Induced Attractive Force	40
<b>Chapter 4</b>	<b>A Potential Non-Thermal Effects in Microwave Sintering</b>	<b>41</b>
4.1	Polarization-Charge Effects in the Quasi-Static Regime	44
4.2	Electric Field Profiles in the Quasi-Static Regime	48
4.3	Attractive Force Density on Spherical Surface	52
4.4	Total Attractive Force between Two Spheres	58
4.5	Potential Significance to Microwave Sintering	61
	<b>Conclusion</b>	<b>64</b>
	<b>Reference</b>	<b>67</b>





## CHAPTER 1

### Review of Relevant Microwave Physics

For decades, there have been plenty of microwave researches both in academia and industrial applications, especially for microwave heating effect. The advantages of microwave heating are non-contact to materials, high power uniformity and high heating rate than conventional heating. These make it an outstanding tool in many disciplines, such as chemical analysis [1-8], food manufacturing process [9-13], pest control in cultural heritage preservation [14-30], impurity inactivation in air-conditioning system [31-34]. Many characteristics of microwave heating, such as power uniformity, heating rate, electromagnetic hotspots, and power penetrability, are already studied thoroughly. However, there are still some physical mechanisms staying unclear or underestimated. In this chapter, some basic microwave physics are presented as fundamental introduction of this dissertation.

#### 1.1 Microwave Heating of Dielectric Materials

In spectra of electromagnetic wave, microwave stands the frequency from 300 MHz to 300 GHz, or the wavelength 1 mm to 1 m [35]. When dielectric materials are irradiated by microwave, they absorb electromagnetic energy from wave fields, transfer to heat, and raise their own temperature, which is called microwave heating effect. The energy-



absorbing efficiency depends on material characteristics. Here, we introduce permittivity (complex number) [36],

$$\varepsilon = \varepsilon' + i\varepsilon'' = \varepsilon'(1 + i\tan\delta) \quad (1.1)$$

where  $\tan\delta$  is loss tangent, the ratio of permittivity real part over imaginary part,

$$\tan\delta \equiv \frac{\varepsilon''}{\varepsilon'}. \quad (1.2)$$

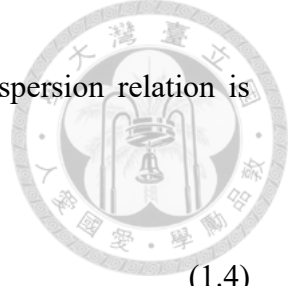
Note that the time dependence of electromagnetic field in this chapter is  $\exp(-i\omega t)$ .

The permittivity real part of a material presents the electric field magnitude of polarization charge. Higher the real part, higher the polarization charge can be induced by the same external electric field. In contrast, the permittivity imaginary part causes power loss of the passing electromagnetic wave, including the influence of both polarization charge and free charge. The power absorption rate per unit volume in a dielectric material ( $p_d$ ) is (Ref. [40], Ch. 7)

$$p_d(\mathbf{x}) = \frac{1}{2}\varepsilon''\omega|E_d(\mathbf{x})|^2 \quad (1.3)$$

where  $\omega$  is the frequency of electromagnetic wave, and  $E_d(\mathbf{x})$  is the electric field at the point  $\mathbf{x}$ .

Because masses of electrons and protons inside dielectric materials are not zero, when frequency of external electric field changes, polarization effect fails to respond simultaneously, resulting in permittivity variation. The relation between permittivity and



radiation frequency is called dispersion relation. In microwave, dispersion relation is given by the Debye function [37-39],

$$\varepsilon(\omega) = \varepsilon(\omega = \infty) + \frac{\varepsilon(\omega = 0) - \varepsilon(\omega = \infty)}{1 - i\omega\tau} \quad (1.4)$$

where  $\tau$  is the temperature-dependent relaxation time. Values of  $\varepsilon(\omega = 0)$ ,  $\varepsilon(\omega = \infty)$  and  $\tau$  can be obtained by a fitting procedure with measured values. For water at 25°C,  $\varepsilon(\omega = 0) = 78.36\varepsilon_0$ ,  $\varepsilon(\omega = \infty) = 5.2\varepsilon_0$  and  $\tau = 8.27 \times 10^{-12}$  (Ref. [38], Table III).

Figure 1.1 displays the permittivity real part and imaginary part separately as a function of frequency.

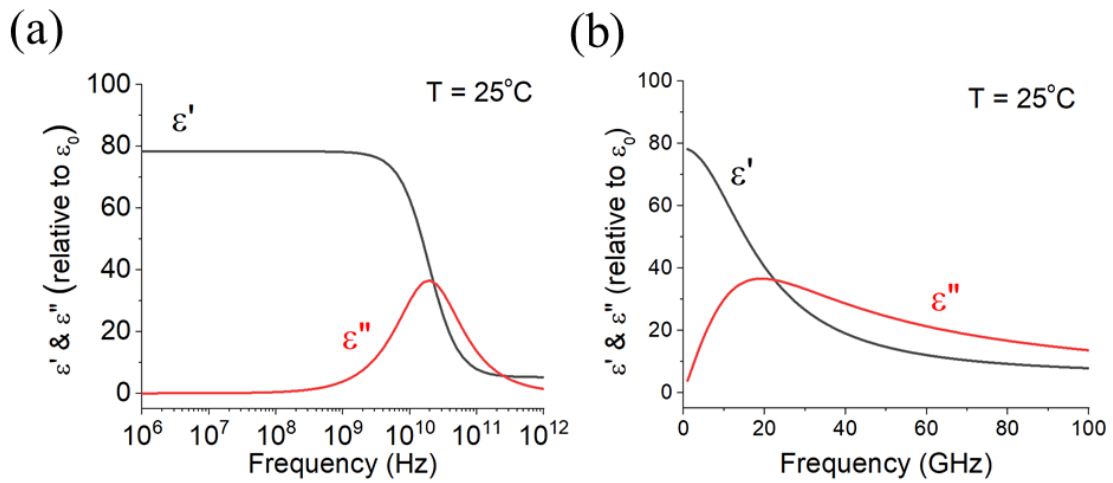
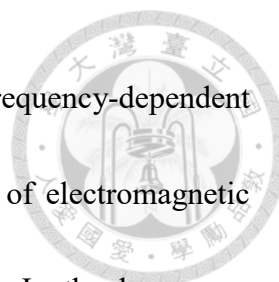


**Figure 1.1:** The permittivity real part and imaginary part of water at 25°C as functions of electromagnetic wave frequency. (a) Frequency from 1 MHz to 1 THz, entire microwave spectra. (b) Frequency from 1 GHz to 1 GHz, main spectra mentioned in this dissertation.



By substituting the above functions into Eq. (1.3), ignoring frequency-dependent variation of microwave electric field inside the water, the relation of electromagnetic power loss  $p_d / |E_d|^2$  and wave frequency is shown in Fig. 1.2. In the low wave frequency regime ( $f < 10$  GHz), the electromagnetic power loss is exponentially positive correlated to frequency, which makes it possible to increase microwave heating rate by raising incident wave frequency. However, it doesn't work in high wave frequency regime ( $f > 10$  GHz). The permittivity imaginary part increases with wave frequency, but the electromagnetic power loss remains almost the same. Frequency increase is independent of microwave heating rate, on the contrary, causing other physical mechanism preventing materials from heating, which will be expounded in next section.

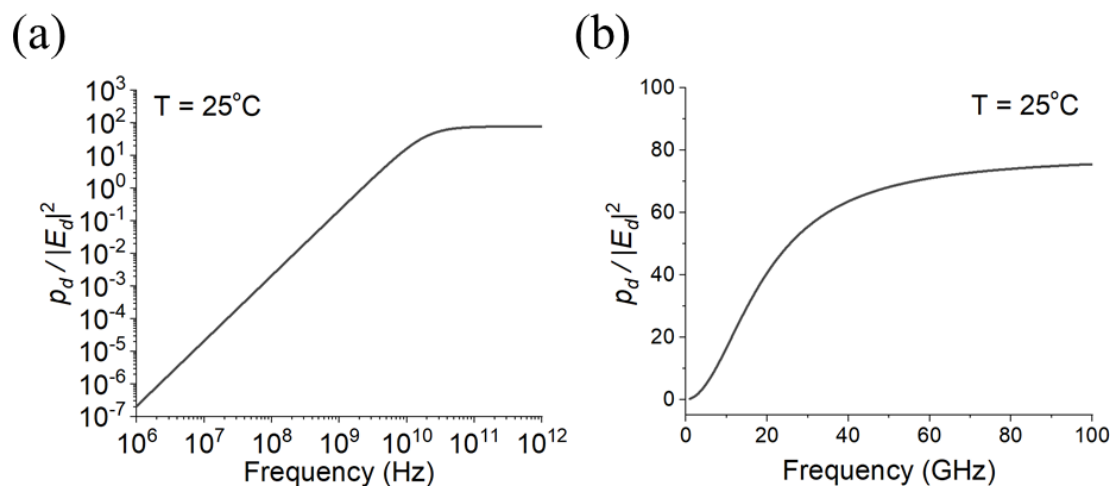


**Figure 1.2:** The electromagnetic power loss  $p_d / |E_d|^2$  of water at 25°C as functions of wave frequency according to Eq. (1.3). The permittivity used here is the same as in Fig. 1.1. (a) Frequency from 1 MHz to 1 THz, entire microwave spectra. (b) Frequency from 1 GHz to 1 GHz, main spectra mentioned in this dissertation.



## 1.2 Penetration Depth

According to Eq. (1.3), to get the maximum microwave heating rate for a certain dielectric material, not only an appropriate electromagnetic wave frequency is necessary, but  $E_d$  (electric field inside the dielectric material) also need to be maximized. When a dielectric material is irradiated by microwave, due to power dissipation caused by its non-zero permittivity imaginary part, the magnitude of electromagnetic field decreases gradually. As the attenuated electromagnetic field is only  $e^{-1}$  of the incident magnitude, the distance which wave has traveled inside the material defines penetration depth. Penetration depth  $d_p$  of a dielectric material can be specified as [40]

$$d_p = \frac{1}{\sqrt{2}} \frac{c}{\omega \sqrt{\frac{\epsilon'}{\epsilon_0}} \sqrt{\sqrt{1 + \left(\frac{\epsilon''}{\epsilon'}\right)^2} - 1}}, \quad (1.5)$$

where  $\epsilon = \epsilon' + i\epsilon''$  and  $\mu = \mu_0$ .

In Fig. 1.3, water at 25°C is presented as an example. In the low wave frequency regime ( $f < 10$  GHz), the penetration depth is negative correlated to wave frequency, power dissipation preventing higher frequency wave field from penetrating. As wave frequency approaches high wave frequency regime ( $f > 10$  GHz), the down trend of penetration depth becomes flattened. However, it has been shortened than 0.1 cm, smaller than most common microwave heating targets like test tubes for chemical synthesis (~1 cm), and microwave power is almost blocked.




Besides, microwave heating rate is higher at high wave frequency as mentioned in last section. In combination with the above conclusion, most part of microwave power concentrates on the surface of heating targets at high wave frequency, leading to the extreme nonuniformity of microwave heating.

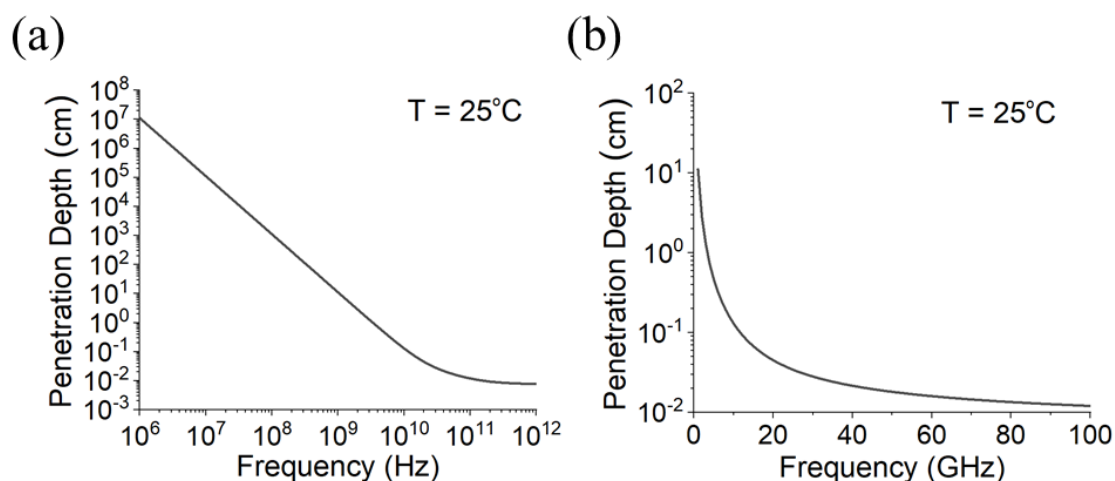


**Figure 1.3:** The penetration depth  $d_p$  of water at 25°C as functions of wave frequency according to Eq. (1.5). The permittivity used here is from Fig. 1.1. (a) Frequency from 1 MHz to 1 THz, entire microwave spectra. (b) Frequency from 1 GHz to 1 GHz, main spectra mentioned in this dissertation.

### 1.3 Shielding Effect in a Uniform Static Electric Field

A dielectric atom is composed of a positive atomic nucleus and several negative electrons around the orbit. In macroscopic view, due to same amount of positive and



negative charges, dielectric materials remain electrically neutral. By applying a uniform static electric field, although electrons on the orbit cannot travel to the direction of external electric field like free electrons, they will be taken apart from the original positions. The separation of nuclei and electrons results in an electric dipole moment, called polarization [41].

Assume a dielectric sphere put in a uniform static electric field  $E_0$ , shown in Fig. 1.4. With opposite charges, nuclei and electrons are driven apart in opposite direction by the external electric field, resulting in positive and negative polarization charge on the right and left sides of dielectric sphere, respectively. Inside the sphere, the electric field due to the polarization charges is oppositely directed to the external electric field, which reduces the internal electric field. It seems that the polarization charges prevent the external electric field from entering the sphere. Hence, this phenomenon is known as a shielding effect.

On the other hand, the electric field from polarization charge and the external electric field are in the same direction outside the sphere, raising the electric field magnitude around the sphere. The magnitude of this electric field intensification depends on permittivity, shape and positions of dielectric materials. Through specific arrangement, this intensified electric field is possible to reach air breakdown strength, which will be further introduced in Chap. 3.



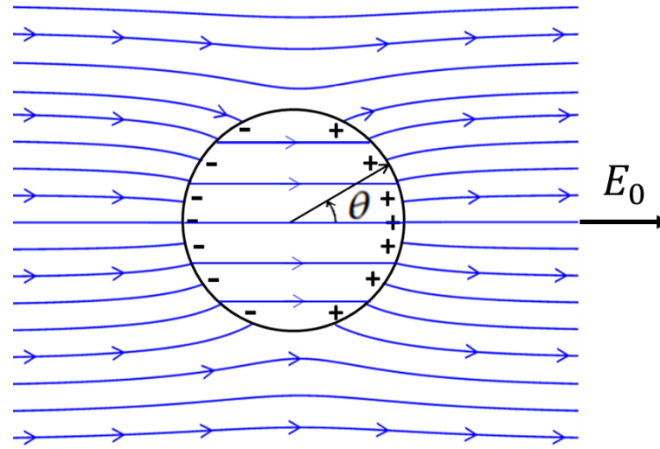


**Figure 1.4:** Schematic diagram of polarization shielding effect of a dielectric sphere in an external uniform static electric field  $E_0$ . Positive nuclei and negative electrons are separated to opposite directions by  $E_0$ , forming polarization charge, which shields  $E_0$  from entering the sphere and strengthens the outside electric field around.

## 1.4 Microwave Resonance in Dielectric Materials

When an electromagnetic wave enters into a dielectric material, wave speed is decelerated and wavelength is shortened. The wavelength in a dielectric material  $\lambda_d$  is given by [Ref. [40], p. 311],

$$\lambda_d \approx \frac{\lambda_{free}}{(\epsilon' / \epsilon_0)^{1/2}} \quad (1.6)$$

where  $\lambda_{free}$  is the wavelength in vacuum, permittivity of the dielectric material

$\epsilon = \epsilon' + i\epsilon''$  and permeability  $\mu = \mu_0$ .

2.45 GHz,  $R = 0.684$  cm

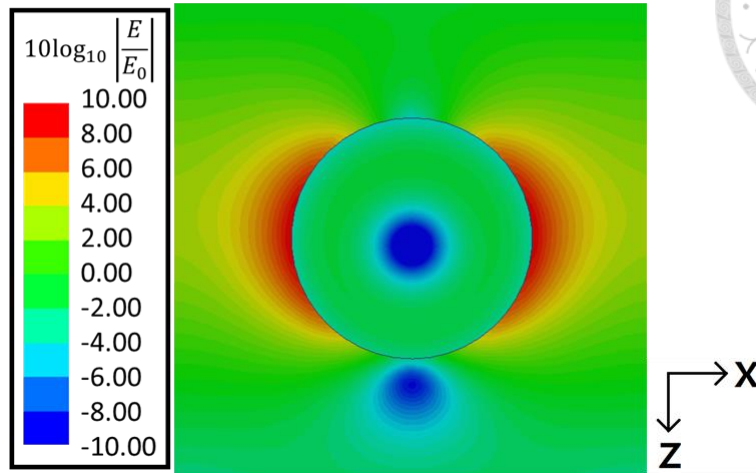
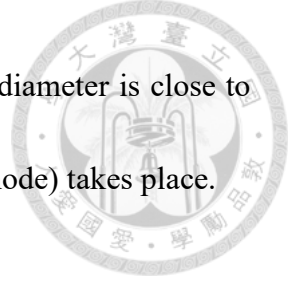


**Figure 1.5:** Simulated electric field magnitude pattern on  $x$ - $z$  plane for a water sphere ( $R=0.684$  cm) at wave frequency 2.45 GHz. The color code gives  $10 \log_{10}[E(\mathbf{x})/E_0]$ .

Meanwhile, when the internal electromagnetic wave strikes the material boundary, refraction and reflection occur due to the permittivity difference of dielectric and vacuum. Under certain boundary condition, reflected and incident wave can be in constructive intervention inside the dielectric material. Hence, make the material act like an electromagnetic resonant cavity.

Here, water at 25°C and a microwave frequency of 2.45 GHz are selected for the example in Fig. 1.5. According to the Debye function [Eq. (1.4)], the wavelength in vacuum is  $\lambda_{free} = 12.24$  cm, and in water is  $\lambda_d = 1.39$  cm. Assume an  $x$ -polarized 2.45-GHz microwave propagates in the  $z$ -direction onto a water sphere with center located at



origin of coordinates and radius  $R$ . With  $R=0.684$  cm, the sphere diameter is close to the wavelength  $\lambda_d$ , and the first electromagnetic resonance (TE11 mode) takes place.

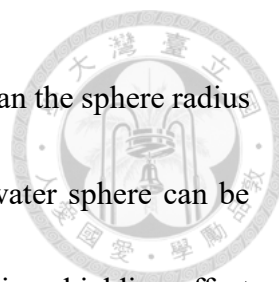
## 1.5 Quasi-static Regime

In section 1.3, polarization shielding effect of dielectric materials in a uniform static electric field is mentioned. Instead of exposure to a static  $E_0$ , dielectric materials are now radiated by a plane microwave. If the microwave frequency is low enough, wavelength in the dielectric is much larger than the sphere radius,

$$\lambda_d \gg R. \quad (1.7)$$

The dielectric sphere falls in the near zone, where  $E_0$  is spatially uniform. The induced fields can thus be approximated by a quasi-static electrical component with a spatial dependence given by static equations (Ref. [40], Sec. 10.1). Hence, all fields oscillate in-phase with  $E_0$ .

Additionally, the first electromagnetic resonance (TE11 mode) inside a water sphere ( $R=0.684$  cm) irradiated by 2.45-GHz microwave is presented in section 1.4. With same radiation condition (linearly polarized in the x-direction propagating in the z-direction) and same water sphere sample, the microwave frequency decreases to 27 MHz from 2.45 GHz. According to the Debye function, the permittivity of water  $\varepsilon = (78.4 + 0.1i)\varepsilon_0$ , wavelength in vacuum  $\lambda_{free} \approx 10^3$  cm, and wavelength in water  $\lambda_d \approx 124$  cm. This 27-



MHz case is in static regime, due to both wavelengths much larger than the sphere radius  $R$ . Shown in Fig. 1.6, the electric field pattern in and around the water sphere can be specified by the approximation of the static equations. The polarization shielding effect prevents the external electric field from entering the sphere just as the static field case.

27 MHz,  $R = 0.684$  cm

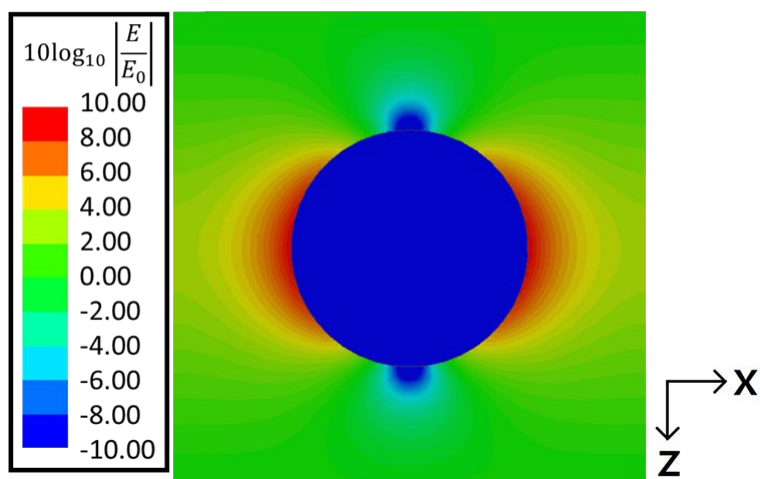


**Figure 1.6:** Simulated electric field magnitude pattern on  $x$ - $z$  plane for a water sphere ( $R=0.684$  cm) at wave frequency 27 MHz. The color code gives  $10\log_{10}[E(\mathbf{x})/E_0]$ . Instead of electromagnetic phenomena, the polarization shielding effect of static electric field dominates.

## CHAPTER 2

### Microwave Phenomena in Dielectrics\*



This chapter considers the following two cases analytically. First, assume a dielectric sphere in a uniform static electric field, and calculate the numerical solution for polarization charge shielding effect. Second, assume a dielectric sphere irradiated by a plane wave. With discrete sphere radii, the dielectric sphere can be an electromagnetic resonant cavity. Then combination of these two effects provides a full physical picture of water responses in variation with the radius, from the quasi-static regime, to electromagnetic resonance regime, and eventually to the wave attenuation regime.

#### 2.1 A Dielectric Sphere in a Uniform Static Electric Field

In Fig. 2.1, assume that a dielectric sphere is placed in vacuum with radius  $R$  and its center is located at the origin of coordinates. Apply a uniform static electric field  $E_0$  with the direction along  $+x$ -axis. The dielectric material of the sphere is uniform and isotropic with permittivity  $\varepsilon_d = \varepsilon' + i\varepsilon'' \simeq \varepsilon'$ . In this case, the permittivity imaginary part can be ignored.

---

\*Analytical expressions in the first two sections of this chapter were obtained in collaboration with Kuan-Wen Chen during his master thesis research [43].

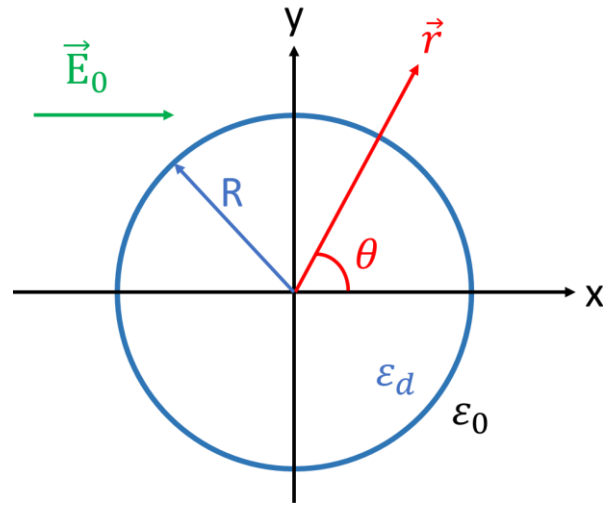


**Figure 2.1:** Schematic diagram of a dielectric sphere ( $\epsilon_d = \epsilon' + i\epsilon'' \approx \epsilon'$ ) in vacuum, with a  $+x$ -direction uniform static electric field.

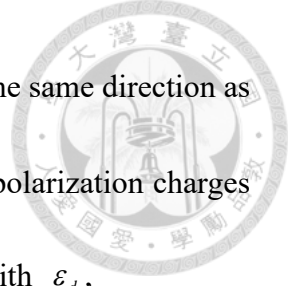
Because of the symmetry of this case, the coordinate is changed from Cartesian to spherical  $[r, \theta, \phi]$ . The electric field inside the sphere ( $r < R$ ) and outside ( $r > R$ ) is labeled with  $\mathbf{E}^-$  and  $\mathbf{E}^+$  respectively, given by (Ref. [40], pp. 157-159)

$$\mathbf{E}^- = \frac{3E_0}{2+\beta} (\cos\theta \mathbf{e}_r - \sin\theta \mathbf{e}_\theta) = \frac{3E_0}{2+\beta} \mathbf{e}_x \quad (2.1)$$

$$\mathbf{E}^+ = E_0 \left[ \left( 1 + \frac{2(\beta-1)R^3}{\beta+2} \frac{1}{r^3} \right) \cos\theta \mathbf{e}_r + \left( -1 + \frac{\beta-1}{\beta+2} \frac{R^3}{r^3} \right) \sin\theta \mathbf{e}_\theta \right] \quad (2.2)$$

where  $\beta$  is the ratio of the dielectric permittivity  $\epsilon_d$  over vacuum permittivity  $\epsilon_0$ ,

$$\beta \equiv \frac{\epsilon_d}{\epsilon_0}. \quad (2.3)$$



According to Eq. (2.1), the electric field inside the sphere is in the same direction as the external E-field, only of smaller magnitude due to shielding by polarization charges on right and left sides of the sphere, which is negatively correlated with  $\varepsilon_d$ ,

$$|\mathbf{E}^-| = \frac{3E_0}{2 + \beta}. \quad (2.4)$$

The electric polarization  $\mathbf{P}$  (total dipole moment per volume) inside the dielectric sphere is specified by

$$\mathbf{P}^- = (\varepsilon_d - \varepsilon_0)\mathbf{E}^- = \frac{3(\beta - 1)}{2 + \beta} \varepsilon_0 E_0 \mathbf{e}_x. \quad (2.5)$$

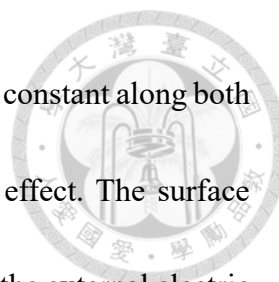
Note that the electric polarization outside the sphere is zero [ $\mathbf{P}^+ = (\varepsilon_0 - \varepsilon_0)\mathbf{E}^+ = 0$ ].

There is no polarization charge inside due to the constant  $\mathbf{P}^-$ . The discontinuous  $\mathbf{P}$  at the boundary of dielectric and vacuum ( $r = R$ ) results in a polarization charge density  $\sigma_{pol}$  on the sphere surface,

$$\sigma_{pol}(\theta) = \frac{3(\beta - 1)}{2 + \beta} \varepsilon_0 E_0 \cos \theta. \quad (2.6)$$

The direction of the electric field caused by  $\sigma_{pol}$  is opposite to  $\mathbf{E}_0$  inside the sphere, which decreases the total internal electric field as a shielding effect. On the contrary, the direction is the same with  $\mathbf{E}_0$  on the central axis ( $x$ -axis) outside the sphere, hence increasing the external electric field.

Use water at 25°C as an example, with  $\beta = 78.4$  according to the Debye function. The magnitudes of electric field along  $x$ -axis and  $z$ -axis are presented in Fig. 2.2. Due to the symmetry of  $y$ - $z$  plane, the results along  $y$ -axis and  $z$ -axis are the same. According to



Eq. (2.3), the total magnitude of internal electric field  $|\mathbf{E}| = 0.037E_0$ , constant along both axes. The magnitude is far less than  $E_0$  because of the shielding effect. The surface polarization charge density is proportional to  $\cos \theta$  and strengthens the external electric field on  $x$ -axis, peak value at  $+x$  and  $-x$  sphere surface, and decaying rapidly with distance.

There is no intensification of electric field along  $z$ -axis outside the sphere.

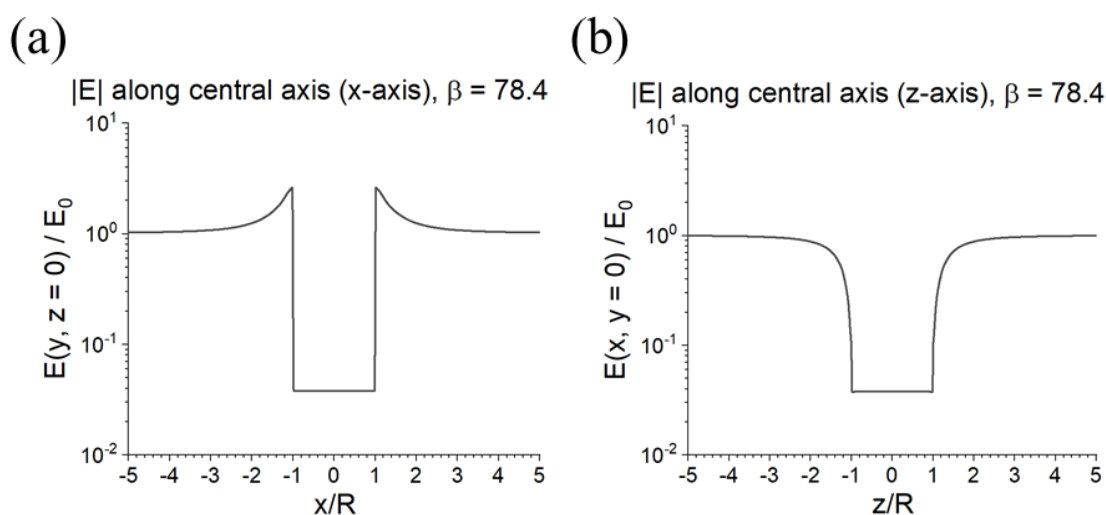
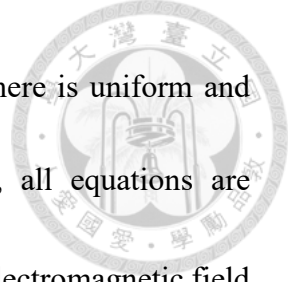


**Figure 2.2:** An illustration of the electric field magnitude around a water sphere with  $\beta = 78.4$  and radius  $R$ . The sphere is in a uniform static electric field with direction in the  $x$ -direction. (a) Profiles of  $E(y, z = 0) / E_0$  along the  $x$ -axis. (b) Profiles of  $E(x, y = 0) / E_0$  along the  $z$ -axis.

## 2.2 A Dielectric Sphere Irradiated by a Plane Wave

In Fig. 2.3, assume that a dielectric sphere is placed in vacuum with radius  $R$  and its center is located at the origin of coordinates. An  $x$ -polarized plane wave is propagating in





the  $z$ -direction toward the sphere. The dielectric material of the sphere is uniform and isotropic with complex permittivity  $\epsilon_d = \epsilon' + i\epsilon''$ . In this section, all equations are expressed in time-harmonic analysis [44], with time dependence of electromagnetic field  $\exp(-i\omega t)$ . The electric and magnetic fields of the incident plane wave are specified as

$$\mathbf{E}^{\text{inc}} = E_0 e^{-ikz} \mathbf{e}_x = E_0 e^{-ikr \cos \theta} \mathbf{e}_x \quad (2.7)$$

$$\mathbf{H}^{\text{inc}} = \frac{E_0}{\sqrt{\mu_0/\epsilon_0}} e^{-ikz} \mathbf{e}_y = \frac{E_0}{\sqrt{\mu_0/\epsilon_0}} e^{-ikr \cos \theta} \mathbf{e}_y, \quad (2.8)$$

where  $E_0$  is the electric field magnitude of incident wave.

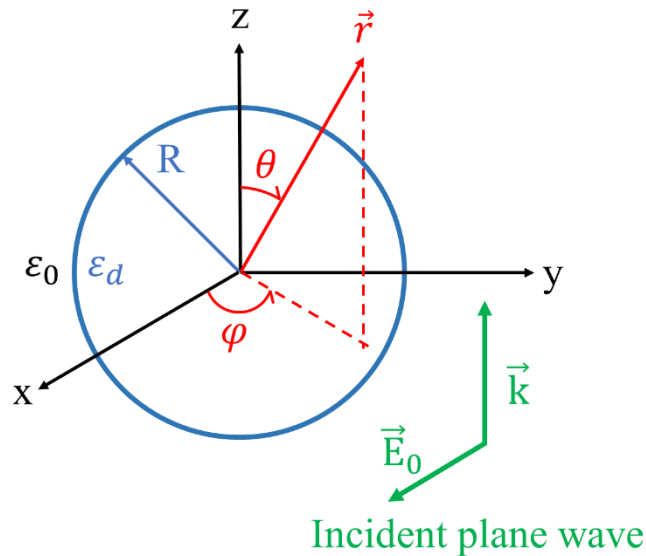
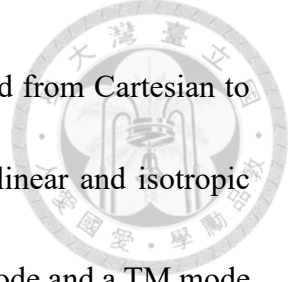


**Figure 2.3:** Schematic diagram of a dielectric sphere ( $\epsilon_d = \epsilon' + i\epsilon''$ ) in vacuum, and an incident plane wave with electric field linearly polarized in the  $x$ -direction, propagating in the  $z$ -direction.



Because of the symmetry of this case, the coordinate is changed from Cartesian to spherical  $[r, \theta, \varphi]$ . In a source-free region with a homogeneous, linear and isotropic medium, the electromagnetic field is expressed as the sum of a TE mode and a TM mode [45]. By assuming these modes to be transverse to  $\mathbf{e}_r$ , the electric field magnitude inside the sphere is approximately expressed by (Ref. [44], Chap. 6)

$$E_r^- = (-i)E_0 \cos \varphi \sum_{n=1}^{\infty} n(n+1) d_n \frac{j_n(k_d r)}{k_d r} P_n^1(\cos \theta) \quad (2.9)$$

$$E_\theta^- \sim iE_0 \cos \varphi \sum_{n=1}^{\infty} d_n \frac{\hat{J}_n'(k_d r)}{k_d r} \sin \theta P_n^{1'}(\cos \theta) \quad (2.10)$$

$$E_\varphi^- \sim iE_0 \sin \varphi \sum_{n=1}^{\infty} d_n \frac{\hat{J}_n'(k_d r)}{k_d r} \frac{P_n^1(\cos \theta)}{\sin \theta} \quad (2.11)$$

where  $k_d$  is the spatial angular frequency in dielectric,  $d_n$  is given by the boundary condition of sphere surface,  $\hat{J}_n'$  and  $j_n$  are the ordinary and spherical Bessel functions, and  $P_n^1 = \partial P_n / \partial \theta$  (a specific Legendre polynomial [46]).

Use a 2.45-GHz incident wave frequency and water at 25°C as an example, with  $\varepsilon_d = 77.5 + 10i$  according to the Debye function. Fig. 2.4 shows the electric field magnitude pattern of the first two resonant modes (TE<sub>11</sub> and TM<sub>11</sub>) in the water sphere. With  $R = 0.684, 0.98$  (sphere diameter close to  $1, 1.5 \lambda_d$ ), the water sphere is treated as an electromagnetic resonant cavity. Electric field enhancement on the +x and -x out sides of the sphere is caused by polarization charges in the quasi-static regime, which will be explained in Chap. 3.

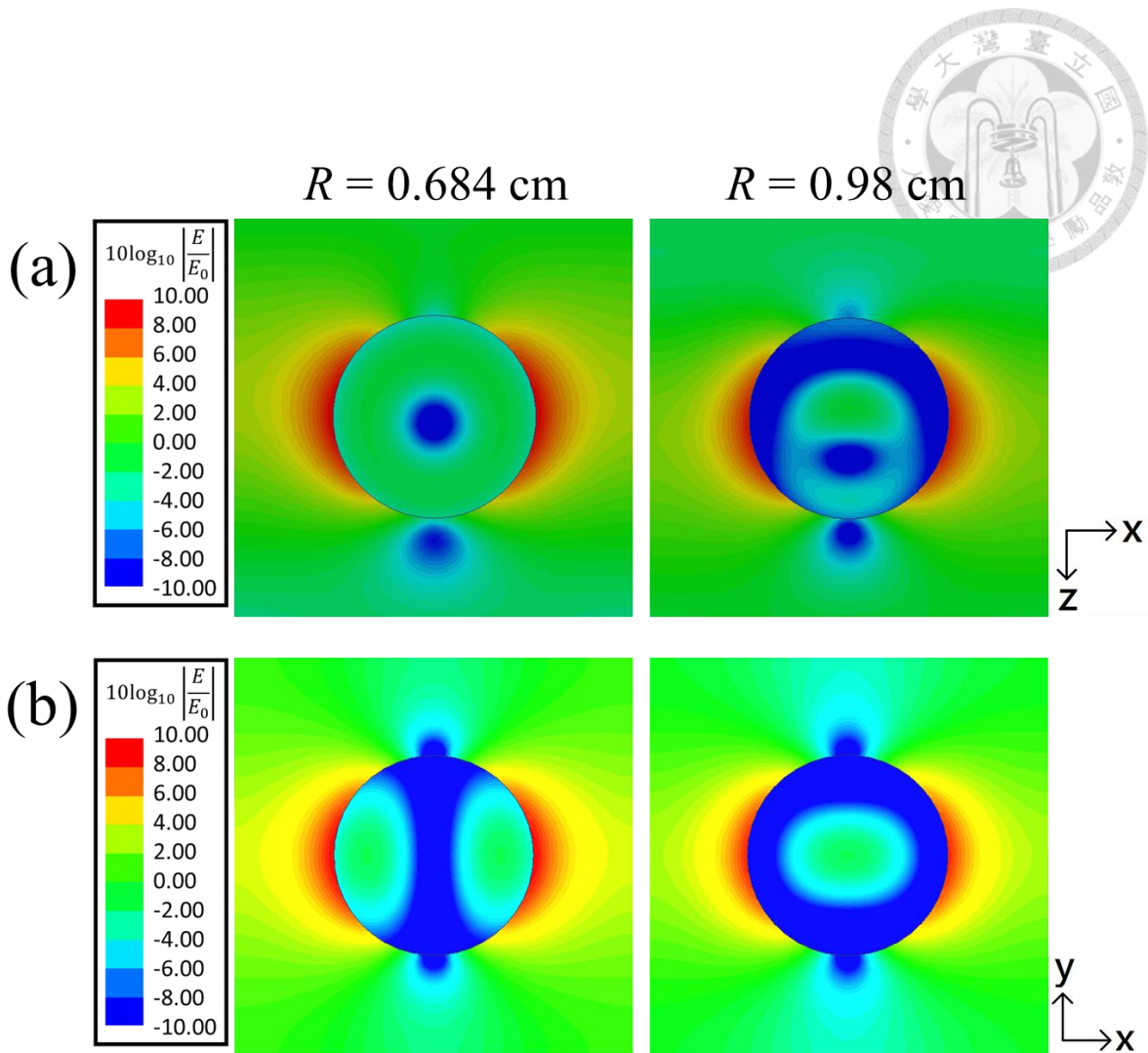
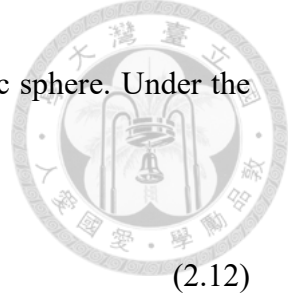


**Figure 2.4:** Simulated electric field magnitude pattern for a water sphere ( $R = 0.684, 0.98$ ) at wave frequency 2.45 GHz. (a) Pattern on x-z plane. (b) Pattern on x-y plane. The color code gives  $10 \log_{10}[E(\mathbf{x}) / E_0]$ .

Now, the field equations are extended to the long-wave-length limit. Consider that the incident wavelength is much greater than the sphere radius  $R$  ( $R \ll \lambda_d$ ), which can be achieved by same spatial scale with low wave frequency or same frequency with small scale. The time dependence remains harmonic ( $\propto e^{-i\omega t}$ ). In contrast, for the spatial



dependence,  $E_0$  is seemed instantaneously uniform in the dielectric sphere. Under the condition:

$$k_d R \ll 1. \quad (2.12)$$

Converting to  $\hat{J}_n'$ ,  $j_n$  and  $P_n^l$  to their explicit expressions the long-wave-length approximations of Eq. (2.9~11) are

$$E_r^- \sim \frac{3}{2+\beta} E_0 \cos \varphi \sin \theta \quad (2.13)$$

$$E_\theta^- \sim \frac{3}{2+\beta} E_0 \cos \varphi \cos \theta \quad (2.14)$$

$$E_\varphi^- \sim \frac{3}{2+\beta} E_0 \sin \varphi. \quad (2.15)$$

Or, in vector form,

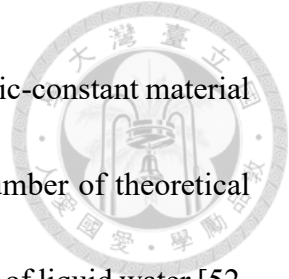
$$\mathbf{E}^-(\mathbf{x}, t) \sim \frac{3}{2+\beta} E_0 e^{-i\omega t} \mathbf{e}_x. \quad (2.16)$$

In the long-wave-length limit, the electric field inside the dielectric sphere is uniform with a decreasing coefficient of  $3/(2+\beta)$ . Apart from the time independence  $e^{-i\omega t}$ , the result is identical to that of the static case [Eq. (2.4)].

### 2.3 Microwave Properties of a Water Sphere

As one of the most abundant substances, water properties are of general interest. In particular, its microwave properties are of importance to both research and applications.

For example, in microwave synthesis, because of the field penetration [47-50], the treatment time is measured in minutes, while the oil-bath method takes hours. The



synthesized solvents are in general water rich. Water is a high-dielectric-constant material with well documented properties (see, for example, Ref. [51]). A number of theoretical and experimental studies have reported the microwave heating effects of liquid water [52-55]. On the other hand, issues related to microwave-assisted chemical synthesis have seldom been examined from the physics perspective.

In previous sections, we have introduced three main properties of dielectric materials: inducing polarization charge in the quasi-static regime (or in the long-wave-length limitation), serving as an electromagnetic resonant cavity when its spatial scale is near internal wavelength, and field attenuation deep side when its spatial scale far exceeds the penetration depth. Now, through the spatial scale variation under the same incident wave frequency, these three properties take turns continuously in field analysis of water.

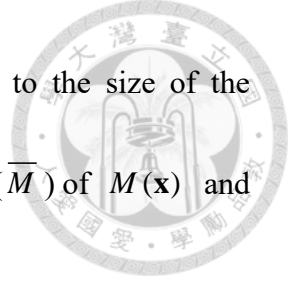
To present heating rate properly, some coefficients are defined first. The power absorption rate per unit volume ( $p_d$ ) in Eq. (1.3) is changed to

$$p_d(\mathbf{x}) = \frac{1}{2} \varepsilon'' \omega |E_d(\mathbf{x})|^2 = \frac{1}{2} \varepsilon'' \omega M(\mathbf{x}) |E_0|^2 \quad (2.17)$$

where  $M(\mathbf{x})$  is the heating-rate modification factor defined as

$$M(\mathbf{x}) = \frac{|E_d(\mathbf{x})|^2}{|E_0|^2} \quad (2.18)$$

Eq. (2.18) provides sufficient information for the evaluation of the local power absorption rate through Eq. (2.17). The polarization-charge shielding and resonance



effects can drastically affect the behavior of  $M(\mathbf{x})$  with respect to the size of the dielectric object. To quantify these effects, we define the mean value ( $\overline{M}$ ) of  $M(\mathbf{x})$  and its standard deviation ( $\sigma_M$ ) as

$$\overline{M} = \frac{\int_v M(\mathbf{x}) d^3x}{\text{total volume}} \quad (2.19)$$

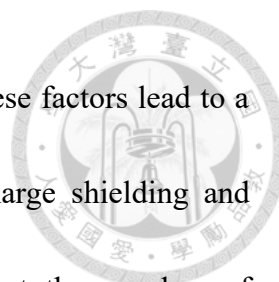
$$\sigma_M = \sqrt{\frac{\int_v [M(\mathbf{x}) - \overline{M}]^2 d^3x}{\text{total volume}}} \quad (2.20)$$

where each integral is over the total volume of the sample under study.

Assume a water sphere at 25°C is radiated by an  $x$ -polarized plane microwave propagating in the  $z$ -direction. For a wave frequency of 2.45 GHz,  $\varepsilon_d = 77.5 + 10i$  according to the Debye function. Fig. 2.5 shows  $\overline{M}$  and  $\sigma_M$  of the water sphere as a function of radius  $R$ .

The variations are divided into three parts, and some general trends are illustrated:

(1) In the quasi-static limit ( $R \ll \lambda_d$ ),  $\overline{M} \rightarrow 0.0014$ , which is in good agreement with the static case shown in Sec. 3.1.  $\sigma_M$  is still negligible with a slow rising rate, an indication of the increasing spatial nonuniformity. (2)  $\overline{M}$  peaks at 0.7 [Fig. 3(a)] and  $\sigma_M$  peaks at 0.25 [Fig. 3(b)] at the first resonance ( $a = 0.684$  cm). This and subsequent few resonances show a rather broad resonant width due to the large loss factor. (3) As  $R$  increases beyond the penetration depth  $d_p$  ( $\sim 1.72$  cm), there is an exponentially weaker penetration of the incident wave into the center, while the densely populated higher-order,



lower-Q resonances overlap into smoother spatial field patterns. These factors lead to a drop of  $\bar{M}$  and  $\sigma_M$  with  $R$ . (4) The combined polarization-charge shielding and resonance effects result in a variation of  $\bar{M}$  and  $\sigma_M$  by about three orders of magnitude over the range of a under consideration.

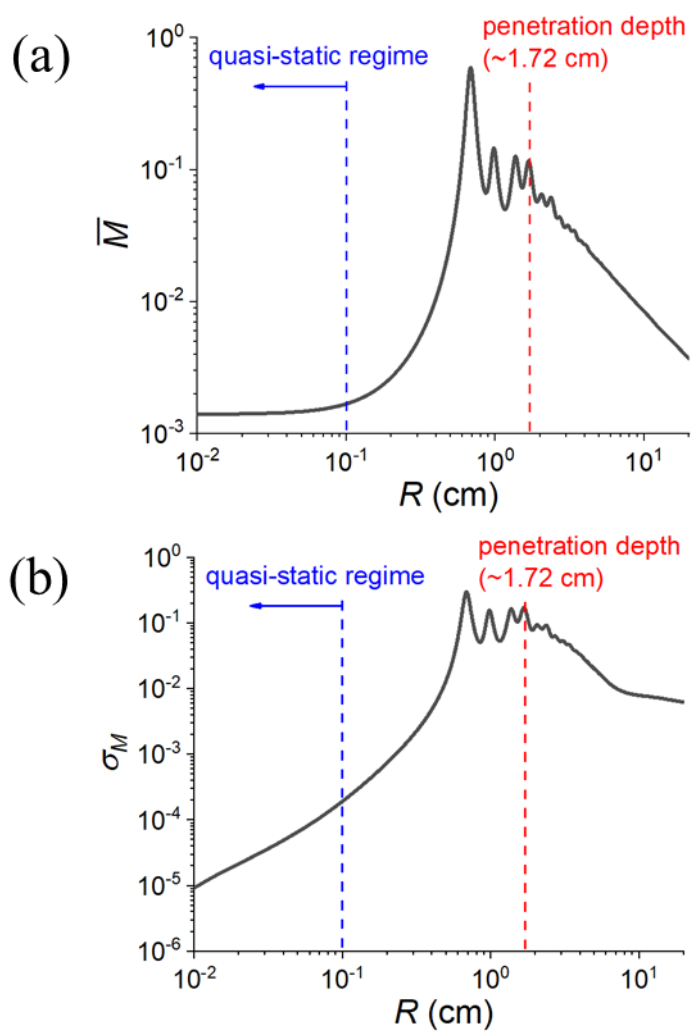


**Figure 2.5:**  $\bar{M}$  and  $\sigma_M$  as functions of  $R$  showing the behavior of the water sphere in the quasi-static regime ( $R \ll \lambda_d$ ), the first few resonances, and the attenuation regime of  $R \gg d_p$ .

These properties are universal over the microwave spectrum. The  $\overline{M}$  variation of 915 MHz, another frequency in ISM radio band, is shown in Fig. 2.6 for comparison. For 915 MHz, the complex permittivity  $\varepsilon_d = 78.2 + 3.5i$  (smaller loss tangent than 2.45 GHz), wavelength in vacuum  $\lambda_{free} = 32.77$  cm ( $>12.24$  cm for 2.45 GHz), and wavelength in water  $\lambda_d = 3.71$  cm ( $>1.39$  cm for 2.45 GHz). As a result, the demarcation line of polarization-charge shielding and resonance effects is in larger spatial scale for 915 MHz, meaning that it is suitable to large-target heating (see, for examples, [5, 6, 8, 12, 13]). By selecting a proper wave frequency, the optimization of microwave heating is possible, for both the heating rate and uniformity.

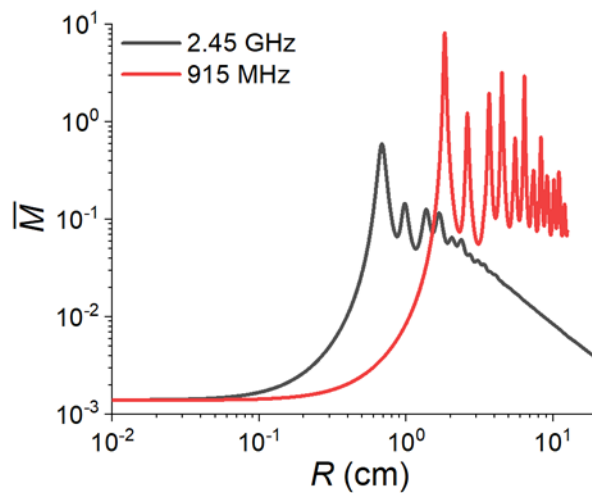
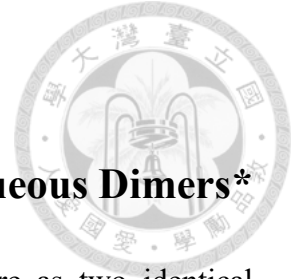


**Figure 2.6:**  $\overline{M}$  of 2.45 GHz and 915 MHz as functions of  $R$  showing the behavior of the water sphere in the quasi-static regime ( $R \ll \lambda_d$ ), the first few resonances, and the attenuation regime of  $R \gg d_p$ .



## CHAPTER 3

### On Electromagnetic Wave Ignited Sparks in Aqueous Dimers\*

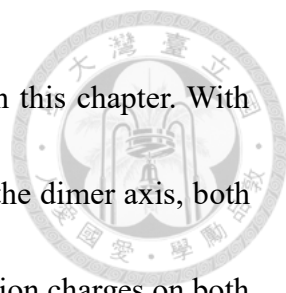


Electromagnetic-wave interactions with a dimer (defined here as two identical dielectric spheres at a close distance) can shed microscopic light to interpret macroscopic matter behaviors of a complex systems. For more than two decades, a popular science puzzle appears in social media, which can serve as a good illustration of such interactions. Inside a household microwave oven, sparks are ignited between a dimer formed of two closely spaced grapes. Khattak's group gave the first scientific interpretation in a PNAS paper in 2019 [56]. They attributed this sparking phenomenon to a hotspot in the gap, which results from the merging of electromagnetic resonances in each half of the dimer. Due to the novelty and public interest of this research, it has been widely reported [57-60].

Although rich in physics, their interpretation to this household puzzle raises fundamental questions. Among them, the claimed demonstration of optical writing with a resolution better than  $\lambda_0/80$  is highly unlikely in such a simple structure. An

---

\* The main research in this chapter was done in collaboration with my junior labmate M. S. Lin during our doctorate degree research. The results are published in *Plasma of Physics* in which I am listed as the co-first authors [61].

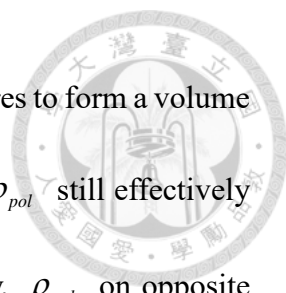


independent interpretation of a much different nature is presented in this chapter. With the same model as in Ref. 56 and an incident wave polarized along the dimer axis, both theory and experiment indicate that mutual enhancement of polarization charges on both sides of the narrow gap can lead to a gap electric field 100s of times greater than that of the wave, hence triggering the sparks through air arcing. The first evidence is the (predicted and observed) sparks at 27 MHz, which provides an essentially magnetic-field free environment. The second evidence is, even under strong dimer resonances at 2.45 GHz, there is still a negligibly small magnetic field in the dimer gap. Furthermore, the electric force causes attractive motion of the two spheres of the dimer as observed in a video display, while a repulsive force due to the radiation pressure is expected if the hot spot is an electromagnetic in nature.

### 3.1 Theory and Experiment at Low Microwave Frequency

In Sec. 2.1, it is shown that a water sphere in a uniform static electric field is populated by induced polarization charges  $\sigma_{pol}$  on the spherical surface [see Eq. (2.6)].  $\pm\sigma_{pol}$  cancels most of the external E-field inside the sphere, while approximately doubling it in the neighborhood of the right and left ends of the sphere.

The situation is markedly different in the gap region between two water spheres aligned side-by-side along  $E_0$  [Fig. 3.1(a)]. First, the induced polarization charges are



no longer exactly on the surface. They penetrate slightly into the spheres to form a volume charge density ( $\rho_{pol}$ ). However, the penetration is so shallow that  $\rho_{pol}$  still effectively resides on the surface as in Eq. (2.6). Second and more importantly,  $\rho_{pol}$  on opposite sides of the gap is of opposite signs (denoted below by  $\pm\rho_{pol}$ ). Facing each other,  $\pm\rho_{pol}$  is mutually enhanced, meaning that more molecules of one sphere is polarized by the action of the other sphere. With a narrower gap, this action is stronger, hence greater enhancement and a greater gap electric field. Even in a household microwave oven, the strength of the mutual enhancement can be 2-3 orders of magnitude for E-field in the gap, which exceeds air breakdown strength and lead to sparks (expounded later).

The frequency of 27 MHz, one in ISM radio band, is chosen as the low-microwave-frequency source. Assume a capacitor composed of two circular plates with central axis on  $x$  axis, 10 cm in radius, 4 cm apart, and applied by 27 MHz AC current. The on-axis electric field,  $E_0$  (in the  $\pm x$ -direction), is almost uniform between the plates. Put two water spheres aligned along  $E_0$ , with radius  $R=7$  mm and separated by a distance  $d=0.5$  mm [showed in Fig. 3.1(a), (b)]. According to Debye functions, the complex permittivity of water at 27 MHz is assumed to be  $\epsilon_d = 78.4 + 0.1i$ , where  $\lambda_d (\approx 124 \text{ cm}) \gg R$  and the fields are quasi-static with a negligibly small magnetic component in the near zone.

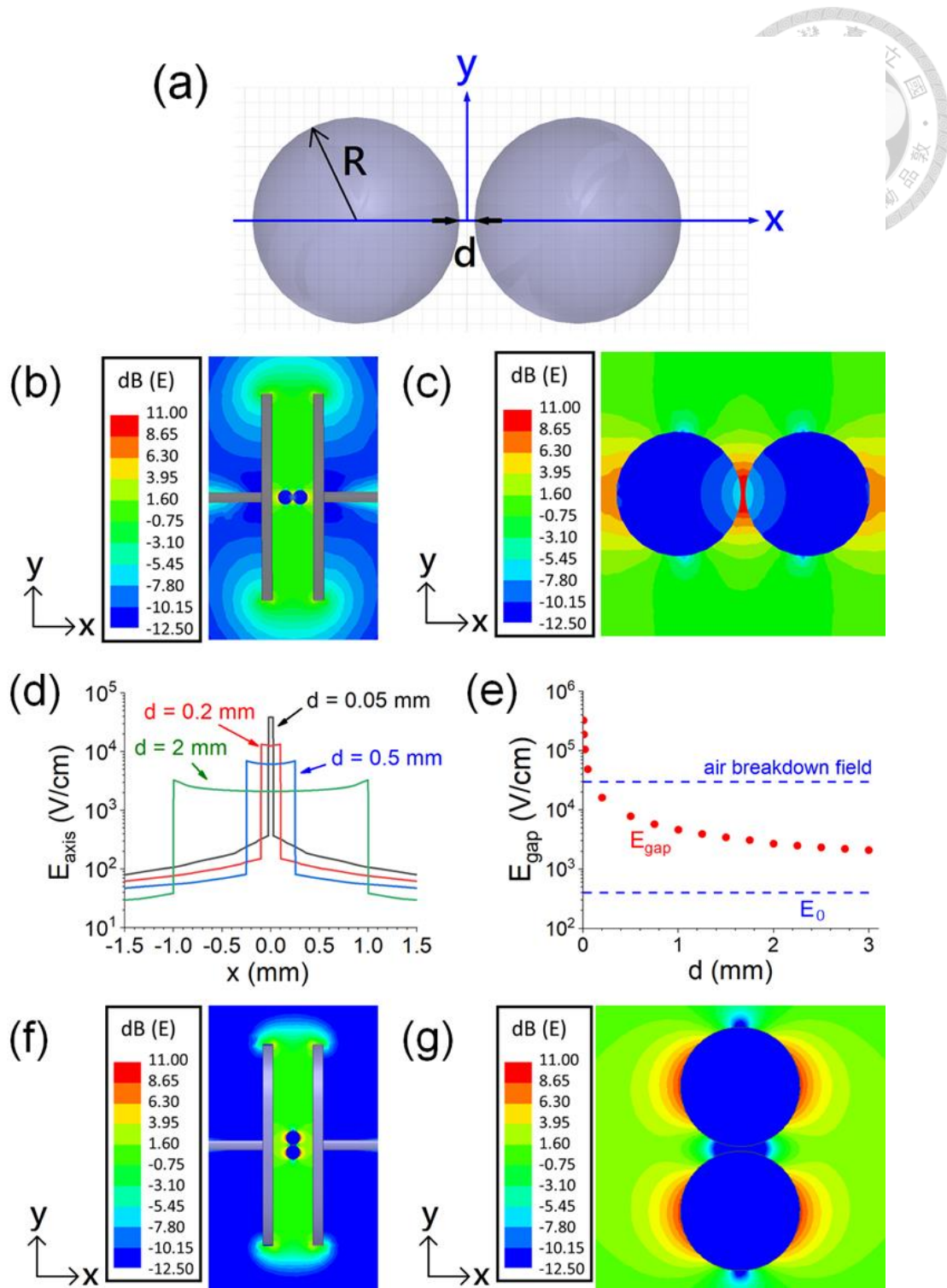


**Figure 3.1:** Simulation model and results at 27 MHz. (a) Model of a dimer. (b) The  $x$ - $y$  plane  $E(x)$  of a capacitor with a  $d = 0.5$  mm dimer along  $E_0$ . (c) Close-up view of the dimer in (b). (d) E-field along the  $x$ -axis. (e)  $E_{\text{gap}}$  vs  $d$ . (f) Results for the dimer rotated by  $90^\circ$ . (g) Close-up view of the rotated dimer.

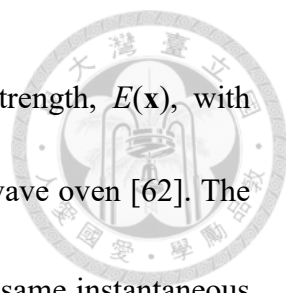


Figure 3.1(b) shows the simulated  $x$ - $y$  plane electric field strength,  $E(\mathbf{x})$ , with  $E_0 = 400$  V/cm, corresponding to the E-field in a household microwave oven [62]. The dimer in Fig. 3.1(c) shows a strong E-field in the gap region. In the same instantaneous  $E_0$ , Fig. 3.1(d) shows the simulation results of the on-axis electric field  $E_{axis}$  along the  $x$ -axis for a dimer with several gap widths  $d$ . For all gap widths  $d$ ,  $E_{axis}$  peaks sharply in the gap region, which is several orders greater than  $E_0$ . For a smaller  $d$ , this enhancement is even more insignificant.

Quantification of the gap electric field strength is denoted by  $E_{gap} = E_{axis}(x=0)$ . Fig. 3.1(e) shows  $E_{gap}$  as a function of  $d$  for  $d = 0.005 - 3$  mm. It can be seen that, at  $d \approx 0.13$  mm,  $E_{gap}$  is equal to the air breakdown strength ( $\sim 3 \times 10^4$  V/cm [63]). Therefore, sparking will be ignited at  $d < 0.13$  mm. Figs. 3.1(c) and 3.1(d) show the E-field energy source resides in the gap region.

Note that even the two spheres in contact ( $d = 0$ ), this physical mechanism still works around the contact point. Without free charges in dielectric material, polarization charges are bound to their respective molecules and fail to move across the contact point in order to neutralization of the dimer. As a result,  $d > 0$  transitions to  $d = 0$  smoothly, so the E-field near the  $d = 0$  point is accurately given by the  $d \rightarrow 0$  data in Fig. 3.1(e). The only limitation is the finite mesh size in simulation.



In comparison, the aligned direction of the dimer is rotated by  $90^\circ$  to make the dimer axis aligned perpendicular to  $E_0$  in Fig. 3.1(f). In the close-up view of the dimer in Fig. 3.1(g), there is no enhancement of the gap electric field. According to Eq. (2.6), when the dimer aligned direction is perpendicular to  $E_0$  ( $\theta = \pm\pi/2$ ),  $|\rho_{pol}|$  is at a minimum near the gap, inducing negligible mutual enhancement.

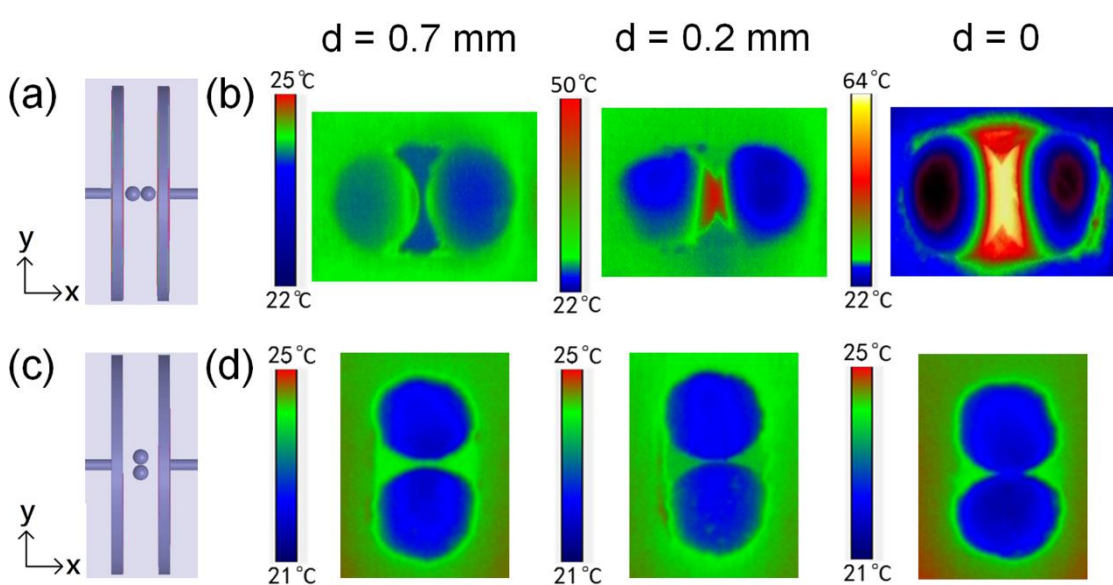


**Figure 3.2:** Configuration and thermal images of the 27-MHz system. (a) The dimer axis is parallel to  $E_0$ . (b) Thermal images of the dimer in (a) for different values of  $d$ . (c) The dimer axis is perpendicular to  $E_0$ . (d) Thermal images of the dimer in (c) for different values of  $d$ . For the experimental data,  $E_0(\text{peak}) = 400 \text{ V/cm}$  with an exposure time of 35 s

This physical mechanism is also verified in experiment (Fig. 3.2). With same dimensions as in simulation, a capacitor is loaded with two  $R=7$  mm hydrogel spheres aligned along  $x$ -axis, parallel to exterior E-field  $E_0$ . To record the experiment, an infrared camera is used to shoot thermal images.

When  $E_0 = 400$  V/cm was applied to the 27-MHz system, arcing between the two spheres simultaneously started, followed shortly by spark ignitions (recorded in the experimental videos [64-66]). However, the gap surface started heated with a little delay to the optically bright sparks. At low wave frequency such as 27 MHz in this case, the conventional AC circuit theory applies to this circuit dimensions. The impedance of the capacitor is  $\sim 1/\omega$ , which is higher at lower frequencies. This may explain the slow heating observed.

Fig. 3.2(b) shows the thermal images of the 27-MHz system after 35-sec exposure to  $E_0 = 400$  V/cm. For all 3 value of  $d$ ,  $T(t = 0) \approx 23.7^\circ\text{C}$  before the exposure. In the case of  $d = 0.7$  mm, the enhanced gap E-field is too small to trigger an arc. At a reduced  $d = 0.2$  mm, the gap starts to arc with  $T$  (spatial maximum of the gap surfaces) =  $41.3^\circ\text{C}$ . For  $d = 0$ , the gap arcs strongly with  $T$  (spatial maximum of the gap surfaces) =  $72.1^\circ\text{C}$ .

With the same capacitor confirmation, the direction of the dimer is rotated by  $90^\circ$  with respect to  $E_0$  [Fig. 3.2(c)] to check whether the gap electric field originates from the

$\pm\rho_{pol}$  buildup. As expected, no elevated temperature is observed [Fig. 3.2(d)] because  $|\rho_{pol}|$  now has a minimum value near the gap [ $\theta = \pm\pi/2$  in Eq. (2.6)].

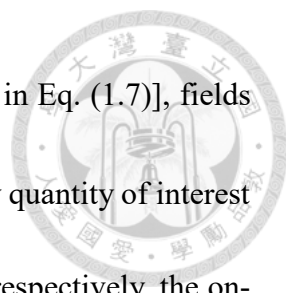
As a conclusion, with negligible magnetic field at 27-MHz environment, the electrical origin for gap sparks can be well-established. Note that E-field intensification has been previously studied for dielectric or conducting dimers in connection with materials processing by microwaves [67-71]. In addition to electrical polarization, multiple effects are involved, making the treated systems more complex. The current model of an isolated dimer reduces the complexity to allow a detailed quantitative study.

### 3.2 Validity Range of the Quasi-static Regime

The electrical arcing mechanism is studied in Sec. 3-1 in 27-MHz system in the quasi-static regime. An important question is whether the electrical arcing mechanism remains valid at higher frequencies when strong electromagnetic resonances take place in the dimer.

To bring out the resonances, we vary the wave frequency ( $f$ ) at a fixed  $R$ . For example, at  $R=7$  mm, the first and second resonances occur at  $\sim 2.45$  GHz and  $\sim 3.4$  GHz, respectively. Assume an  $x$ -polarized plane wave propagating in the  $z$ -direction and denote its E-field amplitude by  $E_0$ . Then, in SI unit, the in-phase magnetic field  $H_0$  has an amplitude given by  $H_0 = E_0/377$ , where 377 is the free-space impedance in Ohm.





At higher frequencies beyond the quasi-static regime [ $\lambda_d \gg R$  in Eq. (1.7)], fields at different points do not oscillate in phase. Nevertheless, the primary quantity of interest is the peak value (amplitude) of the field. Let  $E_{axis}$  and  $H_{axis}$  be, respectively, the on-axis electric and magnetic field amplitudes. For a dimer with  $d = 0.2$  mm, Fig. 3.3(a) plots  $E_{axis} / E_0$  and  $H_{axis} / H_0$  as functions of  $x$  for  $f = 10$  MHz, 1 GHz, and 1.5 GHz. Compared with the size of the dimer, the gap is a narrow region in the figure, where only  $E_{axis} / E_0$  peaks sharply and  $E_{axis} / E_0 \gg H_{axis} / H_0$  in the whole range.

With an in-water wavelength of  $\lambda_d > 23$  mm, the frequency range in Fig. 3.3(a) ( $f < 1.5$  GHz) satisfies the quasi-static condition  $\lambda_d \gg R$  ( $= 7$  mm). Therefore, the dimer is essentially dominated by a static E-field independent of wave frequency  $f$ . For example, 27 MHz is deep in the quasi-static regime. Its field profile will be indistinguishable from that at 10 MHz in Fig. 3.3(a) (also true in Fig. 3.4 below).

Figures 3.3(b)–3.3(d) plot  $E_{axis} / E_0$  and  $H_{axis} / H_0$  for  $d = 0.2$  mm and  $f = 2.45, 6,$  and 10 GHz, respectively. When  $f$  rises above  $\sim 1.5$  GHz, resonant modes start to appear [see Figs. 3.3(b)–3.3(d) for the  $x$ -axis profiles of these modes], under which the gap field is formed of the polarization-charge field and fringe E-fields of the resonances. Nonetheless, the polarization charge may be readily identified as part of the field. On both sides of the gap, the electric field drops steeply, indicating a large  $x$ -gradient of  $E_{axis}$ , or the presence of polarization charges on the gap surfaces. Consequently, surface



polarizations charges are the predominant reason for the sharp peak of  $E_{axis}$  in the gap region.

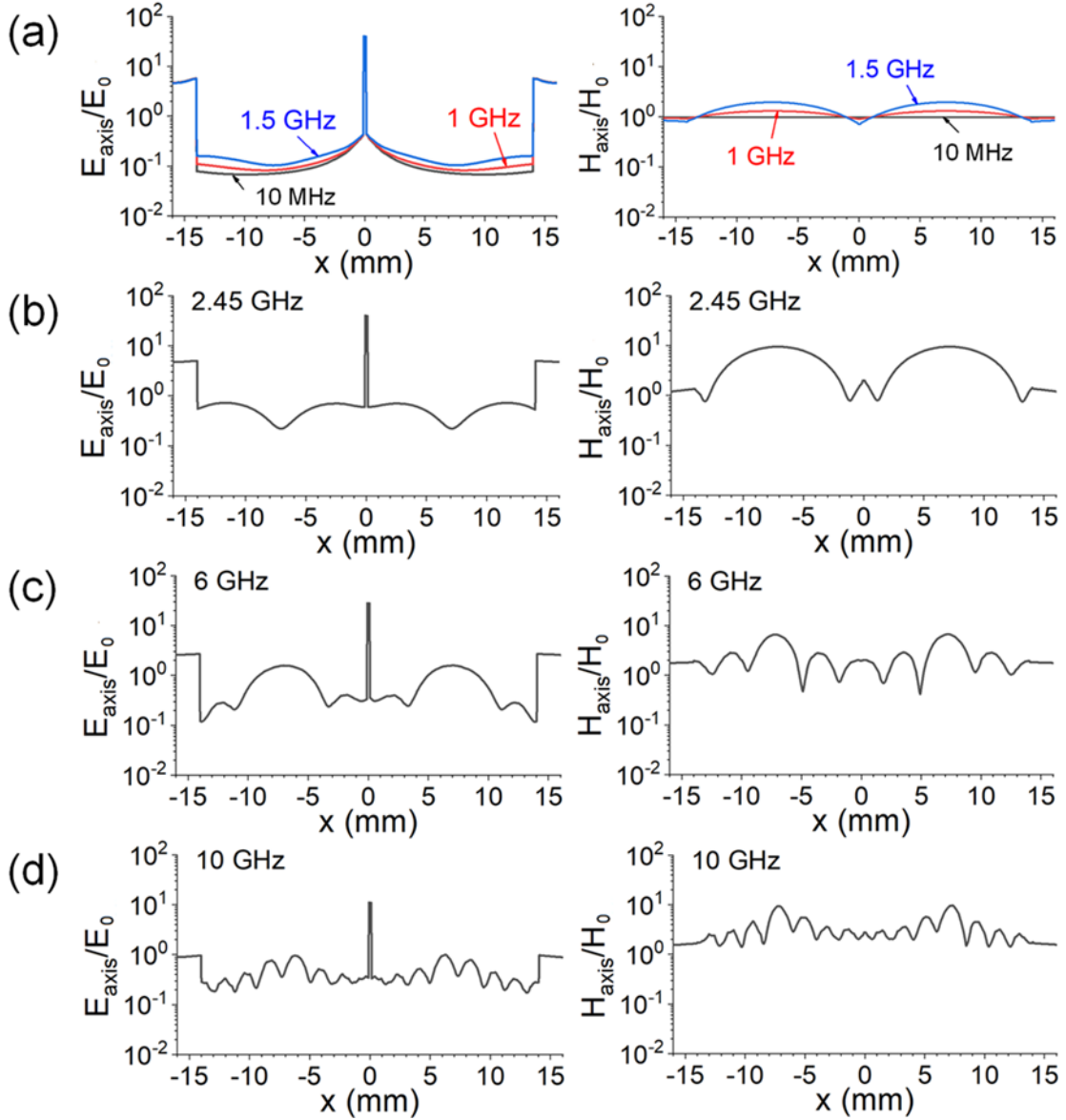


**Figure 3.3:**  $E_{axis} / E_0$  and  $H_{axis} / H_0$  versus  $x$  for a dimer with  $R=7$  mm and  $d = 0.2$  mm under microwave radiation while aligned along  $E_0$ . (a)  $f = 10$  MHz, 1 GHz, and 1.5 GHz. (b)  $f = 2.45$  GHz. (c)  $f = 6$  GHz. (D)  $f = 10$  GHz. For all data,  $E_0 = 400$  V/cm,  $H_0 = 1.06$  A/cm and  $\varepsilon(\text{dimer}) = (77.5 + 10i)\varepsilon_0$ .

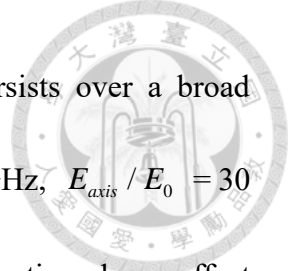
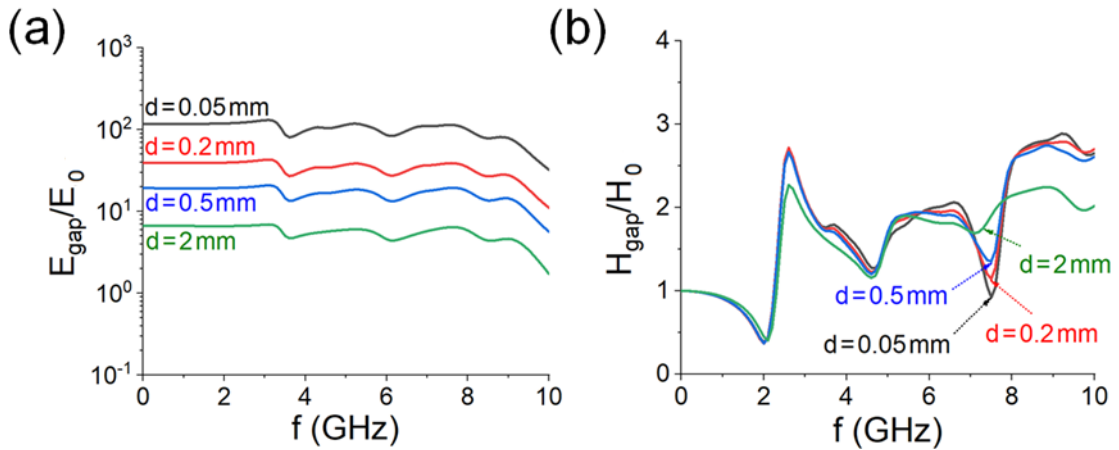
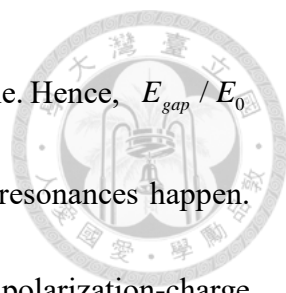


Figure 3.3 also shows that the polarization-charge effect persists over a broad frequency range. Inside the gap, we find  $E_{axis} / E_0 = 40$  at  $f < 2.45$  GHz,  $E_{axis} / E_0 = 30$  at  $f = 6$  GHz, and  $E_{axis} / E_0 = 12$  at  $f = 10$  GHz. As a result, the polarization-charge effect does not significantly fade away until  $f > 10$  GHz.

We may also find quantitatively how the gap polarization-charge field is influenced by sphere resonances. For simplicity, we quantify the gap field by defining  $E_{gap} = E_{axis}(x=0)$  and  $H_{gap} = H_{axis}(x=0)$ .  $E_{gap} / E_0$  and  $H_{gap} / H_0$  versus  $f$  are displayed in Figs. 3.4(a) and 3.4(b), respectively, from 10 MHz to 10 GHz for four values of  $d$ . The fringe E-field of the resonances can be seen in Fig. 3.4(a) to cause only small fluctuations of the smooth polarization-charge field.



**Figure 3.4:** Simulated gap electric field  $E_{gap} / E_0$  versus  $f$  in log scale (a) and gap magnetic field  $H_{gap} / H_0$  versus  $f$  in linear scale (b) for four values of  $d$ .  $f$  ranges from 10 MHz to 10 GHz. The dimer is on the  $x$ - $y$  plane with its axis aligned along  $E_0$  and  $\varepsilon(\text{dimer}) = (77.5 + 10i)\varepsilon_0$ .



At low frequencies ( $f < 1.5$  GHz), we are in the quasi-static regime. Hence,  $E_{gap} / E_0$  is independent of  $f$ . When frequencies rise higher, electromagnetic resonances happen. There is a positive or negative influence of the fringe fields on the polarization-charge field. For example, in the region  $f \sim 3$  GHz,  $E_{gap} / E_0$  maximizes. the fringe fields add a 0.45–3.4% to the polarization charge field. Therefore, there is a minor contribution to the gap E-field even in the strong electromagnetic resonances.

### 3.3 Theory and Experiment at High Microwave Frequency

To verify the electrical nature of the sparks in the presence of electromagnetic resonances, a 2.45-GHz,  $x$ -polarized microwave is input from a rectangular horn antenna along the  $z$ -direction onto a dimer aligned parallel to  $E_0$  [Fig. 3.5(a)]. The dimer, at a distance of 13 cm in front of the antenna opening, is composed of two  $R = 7$  mm water spheres with a variable  $d$ . The incident power varies only  $\sim 1\%$  over the dimer. Hence, it is well represented by its value at the dimer center.

Fig. 3.5(a) plots the simulated instantaneous  $x$ - $z$  plane electric field pattern, and Fig. 3.5(b) plots the  $x$ - $y$  plane electric field amplitude patterns around the dimer for  $d = 2, 1,$  and 0.2 mm. As mentioned in Sec. 2.3, electromagnetic resonance occurs in each sphere, with the following two important features.

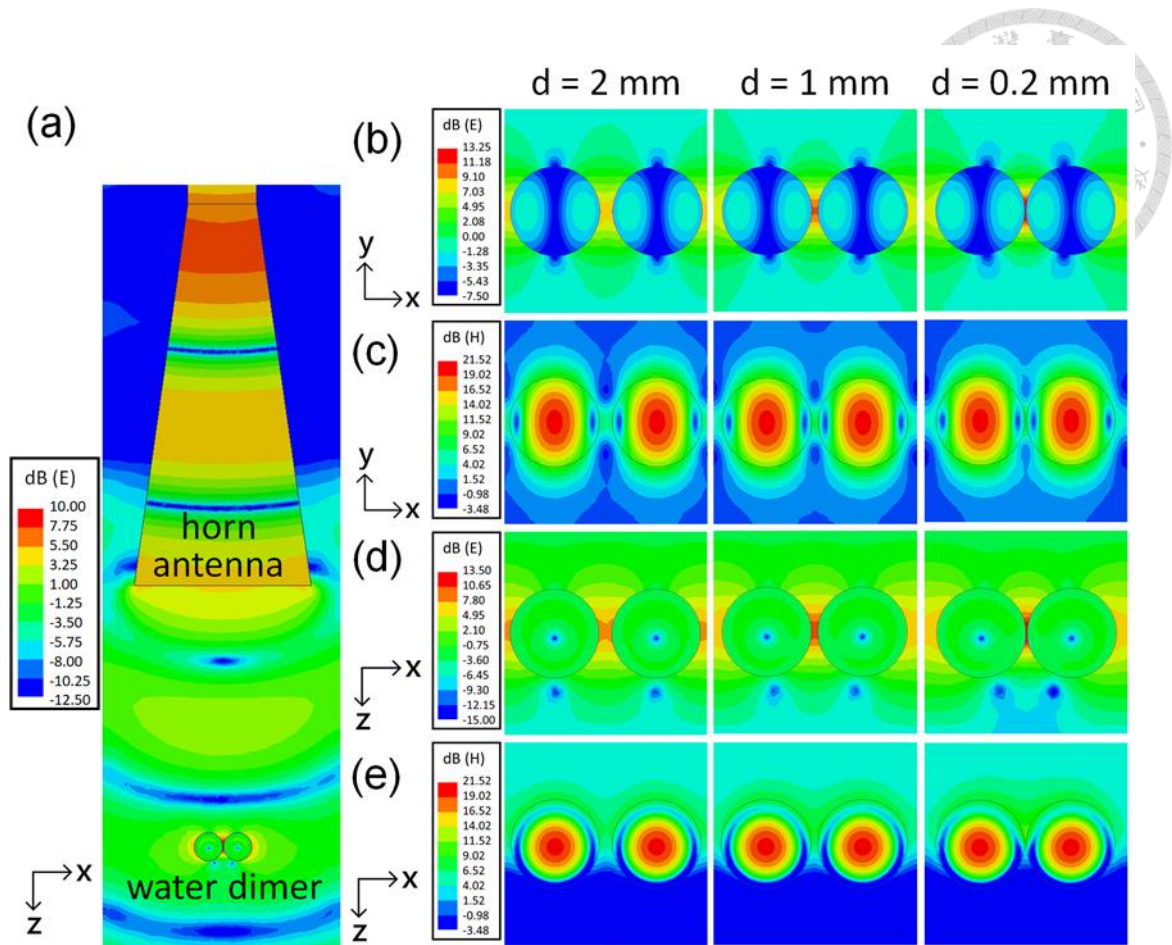


**Figure 3.5:** Simulation results at 2.45 GHz for a dimer oriented aligned along  $E_0$ . (a) The simulation model and E-field pattern on the  $x$ - $z$  plane. (b) The  $x$ - $y$  plane E-field amplitude pattern near the dimer for three gap widths. (c) Corresponding  $x$ - $y$  plane H-field amplitude pattern of (b). (d) The  $x$ - $z$  plane E-field amplitude pattern near the dimer for three gap widths. (e) Corresponding  $x$ - $z$  plane H-field amplitude pattern of (d). For all figures, the dimer with  $\varepsilon(\text{dimer}) = (77.5 + 10i)\varepsilon_0$  is exposed to  $E_0 = 400 \text{ V/cm}$ .

1. At a small  $d$ , we find negligible change of the resonant field pattern and strength within each sphere [Figs. 3.5(b)-(e)] and the gap H-field is negligibly small [Figs. 3.5(c) and 3.5(e)]. Thus, the two resonant modes do not merge into a hotspot in the gap. This is



expected because the resonant mode has a fixed standing wave structure with respect to the sphere boundary.

2. Second, in contrast to the gap H-field, the gap E-field increases sharply as  $d$  decreases [Figs. 3.5(b) and (d)], a display of polarization-charge enhancement. Hence, the incident wave has induced a large polarization-charge E-field in the gap, in addition to generating electromagnetic resonances in the two spheres.

As an additional note, the above results are for a dimer oriented  $E_0$ . Other relative orientations between the aligned direction of the dimer and  $E_0$  have been examined previously. When these two directions are parallel, the gap electric field is at its maximum.

In an over-moded cavity, the strength and direction of  $E_0$  vary randomly and are highly load-dependent (see Fig. 2 of Ref. 62). Hence, the sparking phenomenon occurs stochastically in a microwave oven [56], resulting in poor data reproducibility. This problem can be remedied by traveling-wave irradiation, which is highly uniform on the sample with a known strength and direction.

This physical mechanism can be verified in experiment. With the same configuration as in Fig. 3.5(a), a  $R=7\text{ mm}$  hydrogel dimer, 13 cm in front of the antenna opening, is aligned along  $E_0$  and irradiated by a 2.45 GHz traveling-wave. Instead of 400 V/cm as in the simulation, we used  $E_0(\text{peak}) = 100\text{ V/cm}$  in the experiment, which is the maximum

output power of our magnetron. Extrapolating from Fig. 3.4(a), arcing takes place only when  $d \rightarrow 0$ .



Thermal images of the dimer are shown in Fig. 3.6(a) for  $d = 0.7, 0.1$  mm, and 0 after a 10-sec exposure to an x-polarized  $E_0(\text{peak}) = 100$  V/cm incident along the  $z$ -direction. Arcing starts at  $d = 0.1$  mm and get stronger at  $d = 0$ . The initial temperature is  $22^\circ\text{C}$  and it reaches a maximum of  $52.7^\circ\text{C}$  for  $d = 0.1$  mm and  $83.2^\circ\text{C}$  for  $d = 0$ . Due to insufficient power, sparks are weak for both  $d = 0.1$  mm and  $d = 0$ , but clearly evidenced by the thermal hotspots on gap surfaces.

To check the wave polarization effect, the direction of the dimer is rotated by  $90^\circ$  on the  $x$ - $y$  plane, with its axis aligned perpendicular to the  $E_0$ . As in the 27-MHz experiment in Fig. 3.2(d), no temperature rise has been observed after a 10-s exposure [Fig. 3.6(b)].

As a final note, thermal image reflects the surface temperature, a hotspot on gap surfaces provides evidence of arcing. However, the surface temperature profile after arcing is far from the actual electromagnetic field profile [e.g., Fig. 3.6(b) here or Figs. 3(b), (e), and (h) in Ref. 56], which is shown in the simulations results in Figs. 3.5(b)–(e) here or Figs. 3(c), (f), and (i) in Ref. 56].

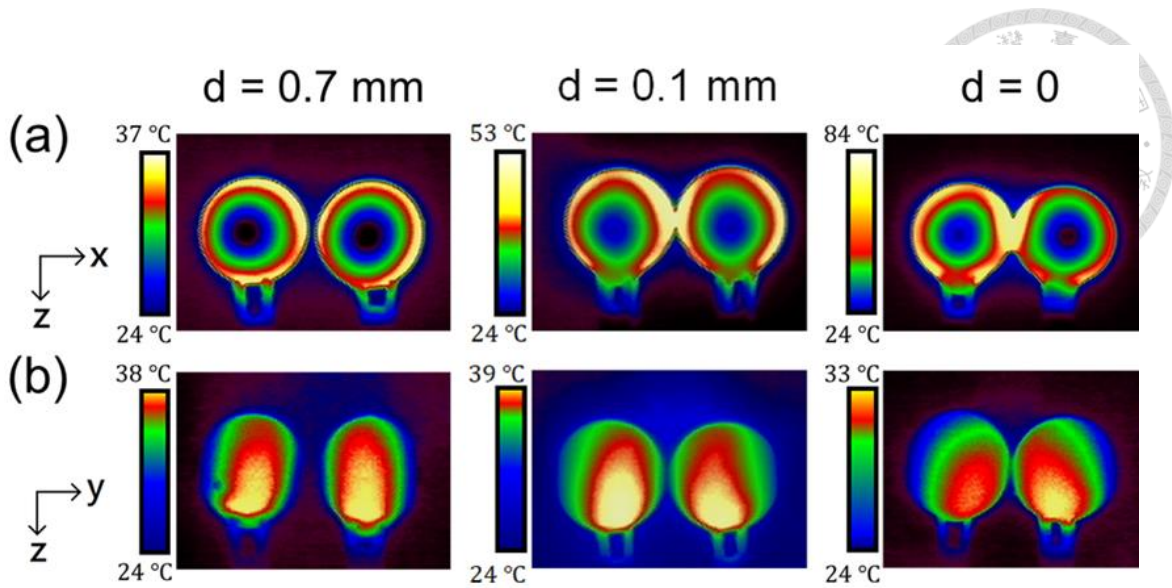


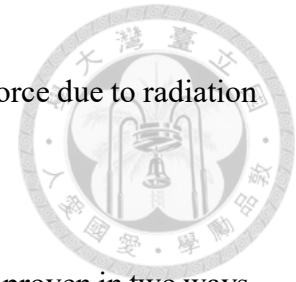
**Figure 3.5:** Experimental thermal images of  $R=7$  mm dimers irradiated by a 2.45-GHz microwave. (a) Thermal image of the surface of the hydrogel dimer aligned along  $E_0$  for three gap widths. (b) Thermal image of the surface of the hydrogel dimer aligned perpendicular to  $E_0$  for three values of  $d$ . For all figures, the  $x$ -polarized  $E_0$  (peak) = 400 V/cm and the exposure time is 10 sec.

### 3.4 Microwave-Induced Attractive Force

In Sec. 3.1, the 27-MHz experiment shows arcing in the gap of the dimer as soon as  $E_0$  applied, followed shortly by spark ignitions [64, 65]. For the 2.45-GHz case, the attractive motion and the eventual sparks is observed in our experimental optical movie [66]. To obtain a greater attractive force and clearer attractive motion, two  $R=10$  mm spheres were placed 2 cm from the horn opening on a horizontal surface. The attraction motion of the two spheres serves as further evidence for the electrical origin of the gap field. The spheres are in strong electromagnetic resonance in the second mode (see Sec.



2.3). If the hot spot were electromagnetic, there would be repulsive force due to radiation pressure.



In summary, the existence of an electrical origin for the sparks is proven in two ways.

(1) It is shown, in both simulation and experiment, to occur at 27 MHz at which no electromagnetic resonance is possible. (2) It is shown, in both simulation and experiment, to occur at 2.45 GHz at which the dimer is in strong resonance. Further, the electrical origin is shown in simulation to persist in the presence of the first few electromagnetic resonances in the dimer. These results shed new light into the basic properties of isolated dimers. It may hopefully be a useful reference for the electromagnetic behavior of complex systems.

## CHAPTER 4

### A Potential Non-Thermal Effects in Microwave Sintering\*



This chapter presents a new interpretation to a general observation in microwave sintering; namely, the processing temperature of microwave sintering is significantly lower than that of the conventional sintering. In thermal processing techniques, sintering is one of the most generally used method to densify fine powders into desired materials [72], with the furnace as the prevalent heat source. From 1960s, the microwave technology advance has originated the microwave sintering field in expectation to its potential advantages. Like mentioned in former researches [73-79], under certain conditions, a large variety of materials are able to be sintered by microwaves. Different from the heating absorption on surface in a conventional furnace, microwave offers the ability of volumetric heating which leads to lower energy consumption, reduced processing time/temperature and rapid heating. Almost all microwave sintering is radiated under the 2.45-GHz frequency. There is even more rapid heating demonstrated with

---

\* The main research in this chapter was done in corporation with my doctorate advisor Prof. Chu. My junior labmate M. S. Lin contributed to part of the cited-literature search. The results are published in *Modern Concepts in Material Science* in which I am the first author [108].

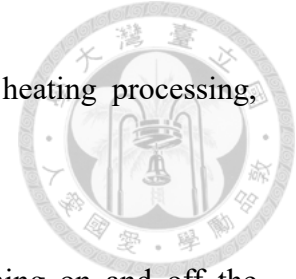


millimeter waves [73, 80, 81]. Still, many problems are found in former studies, such as thermal runaways and sample fractures [82-87]. By now, microwave heating still needs better controlled and characterized to be accepted in more industrial applications.

Researching for decades, many fundamental microwave mechanisms have been interpreted and involved. The basic physical theory of microwave heating has been well documented (Refs. [73-75]). For instance, rapid heating is originated from its volumetric heat deposition. However, there is still a significant difference not fully understood between treatments by the microwave and the one by the conventional furnace. Lots of experiments have shown that a notably reduced processing temperature is required for microwave sintering [73-79, 88-93]. For instance, the research of Brosnan's crew presented the comparison between microwave and conventional methods for alumina sintering. To reach 95% density, the microwave heating processing only needed 1,350°C, which is about 250°C lower than by conventional heating [88]. The reasons for the temperature difference are still unclear, maybe originated from some microwave effects (or non-thermal effects) induced specifically by the electromagnetic fields (Refs. [74-77]). As still an open subject, researchers have proposed some interpretations to recognize the ponderomotive diffusion mechanism.

In a sequence of theoretical and experimental investigations [94-96], the strength of microwave ponderomotive force on the material boundary surfaces is strong enough to

boost mobile ion transport in solids during ceramic microwave heating processing, leading an enhanced mass transport and reaction rate.



In a hybrid conventional/microwave furnace, by only switching on and off the microwave source, Wroe's crew presented that microwave heating decrease the sintering temperature [97]. They concluded that the microwave field on the grain boundary induced the space charge, resulting this sintering enhancement, which discriminatorily enlarged the driving force for grain boundary transport. An exterior magnetic field is also beneficial to the sintering process of magnetic materials [98, 99]. The inward magnetic force may be caused by the polarization current or the wave magnetic field inside a dielectric material [100].

A theory is proposed by the University of Maryland group that a much greater electric field can be induced in the gap region of two close dielectric spheres under microwave radiation [101]. This intensified gap field can result in plasma generation and ponderomotive diffusion, therefore leading to a higher mass transfer rate. Besides, through simulation and experiment, the high temperature from E-field intensification boosts the solid-material fusing and the mass transportation demonstrated by Qiao' group [102].

The electric field intensification effect has also been applied elsewhere. For instance, a chemical reaction or discharge can be motivated by the intensified E-field between

carbon particles [103, 104]. Between two catalyst particles in a solvent, intensification of electric field has been considered in relation to microwave-assisted chemical synthesis [105, 106]. As mentioned in Chap. 3, this effect is also the key to the decades-long, popular-science puzzle in the form of sparks ignited by the electromagnetic wave in the gap of two grapes in a commercial household microwave oven [61, 107].

Despite a verity of former research, the non-thermal effect in microwave sintering still needs further understanding. In this chapter, a different candidate is proposed; namely, the attractive force between two sintered particles caused by the intensification of gap electric field. This microscopic interaction can shed light to the macroscopic behavior of a complex system of fine particles under microwave radiation (see Ref. [101]).

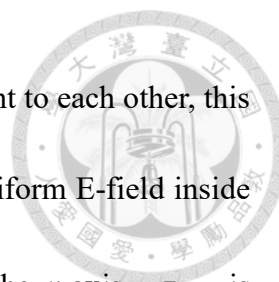
#### 4.1 Polarization-Charge Effects in the Quasi-Static Regime

To simplify the electromagnetic phenomenon in dielectric microwave sintering, we start with the polarization-charge effects of the static case under an uniform electric field and rewrite Eq. (2.4), (2.6),

$$|\mathbf{E}^-| = \frac{3E_0}{2 + \beta} \quad (2.4)$$

$$\sigma_{pol}(\theta) = \frac{3(\beta - 1)}{2 + \beta} \varepsilon_0 E_0 \cos \theta. \quad (2.6)$$

Figure 4.1(a) shows the electric field pattern for a dimer composed of two dielectric spheres with  $\varepsilon/\varepsilon_0 = 20$ . The gap distance between these two spheres is far enough ( $d/R$



= 2) that there is only negligible coupling. Due to spheres independent to each other, this case can be treated as a single sphere with an induced  $\sigma_{pol}$  and a uniform E-field inside the sphere ( $E_{in}\mathbf{e}_x \equiv \mathbf{E}^*$ ), same interpretation in Sec. 2.1. About the  $x$ -axis,  $\sigma_{pol}$  is symmetric, negative on left half of the spherical surface ( $\pi/2 < \theta < \pi$ ) and positive on the right half ( $0 < \theta < \pi/2$ ) with a maximum  $|\sigma_{pol}|$  at  $\theta = 0$  and  $\pi$ . Due to the shielding by the induced  $\pm\sigma_{pol}$ , the  $E_{in}$  in Eq. (2.4) is much reduced from  $E_0$ .

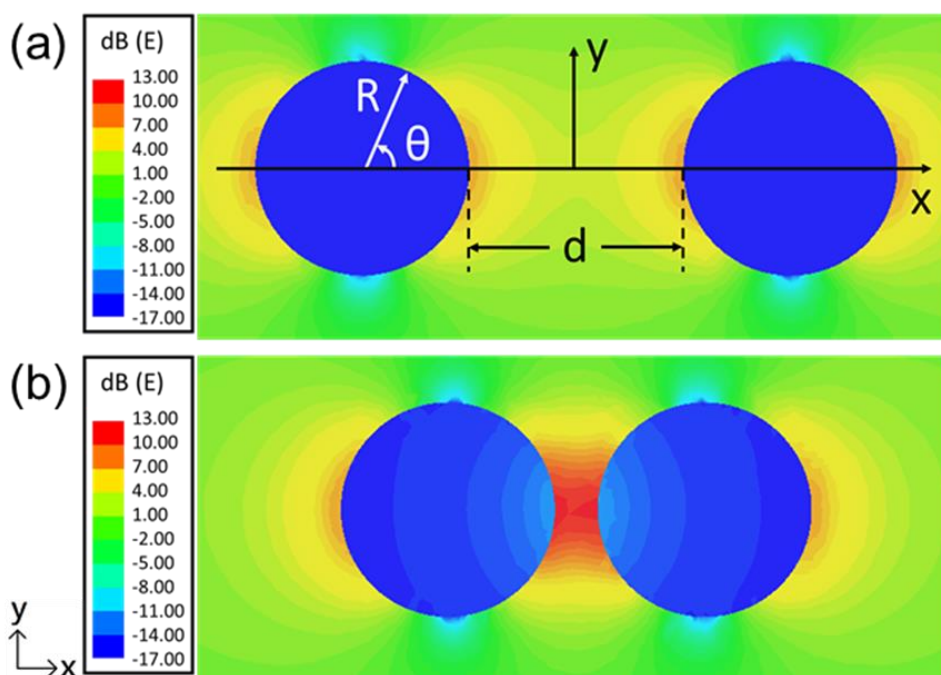
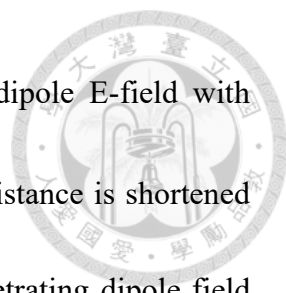


**Figure 4.1:** The  $x$ - $y$  plane electric field pattern of two identical dielectric spheres under  $E_0\mathbf{e}_x$  (uniform static exterior electric field). The dielectric permittivity  $\varepsilon/\varepsilon_0 = 20$ , and sphere radius is  $R$  with gap distance  $d$ . The centers of the two spheres is located on  $x$ - $y$  plane (at  $z = 0$ ). (a)  $d/R = 2$ ; (b)  $d/R = 0.4$ . The color code gives  $\log_{10}(E/E_0)$ .



Outside the sphere, surface charges  $\pm\sigma_{pol}$  produce a pure dipole E-field with decreasing strength away from the sphere. In Fig. 4.1(b), the gap distance is shortened ( $d/R = 0.4$ ). The molecules of one sphere are polarized by the penetrating dipole field from the other, and vice versa. Therefore, polarization charges on the surfaces facing the gap are mutual enhanced. More the gap distance  $d$  narrows, more polarization-charge field penetrates into each other, which leads more  $\pm\sigma_{pol}$  enhancement. As a result, a much higher electric field is inside the gap of the dimer.

For the same two spheres as in Fig. 4.1, the gap distance is now greatly decreased ( $d/R \ll 1$ ) in Fig. 4.2(a). Instead of exposure to a static uniform exterior E-field  $E_0$ , a 2.45 GHz plane wave, propagating downward in the  $-\mathbf{e}_y$  direction with linearly-polarized in the  $x$ -direction, is operated on the dimer. Note that the propagating is now in  $y$ -direction, different from the  $z$ -direction in previous chapters. Because the electromagnetic wavelength in the dielectric is much larger than  $R$  ( $R \ll \lambda_d$ ), the induced fields are dominated by a quasi-static electrical component with a spatial dependence well approximated by that of the static equations (see Sec. 1.5).

To check the quasi-static limitation, we assume that material permittivity  $\varepsilon$  is a real number due to the small imaginary part causing only negligible influence. Denote the E-field inside the gap by  $E_{gap}$ .  $E_{gap}(x=y=0)/E_0$  as functions of  $R$  for  $\varepsilon/\varepsilon_0 = 20$  ( $\lambda_d = 2.74$  cm) is showed in Fig. 4.2(b) with several different  $d/R$ . For a fixed  $d/R$  up to



$R \approx 0.5$  cm, the E-field is essentially independent of  $R$  which can be treated as the borderline of the quasi-static regime.

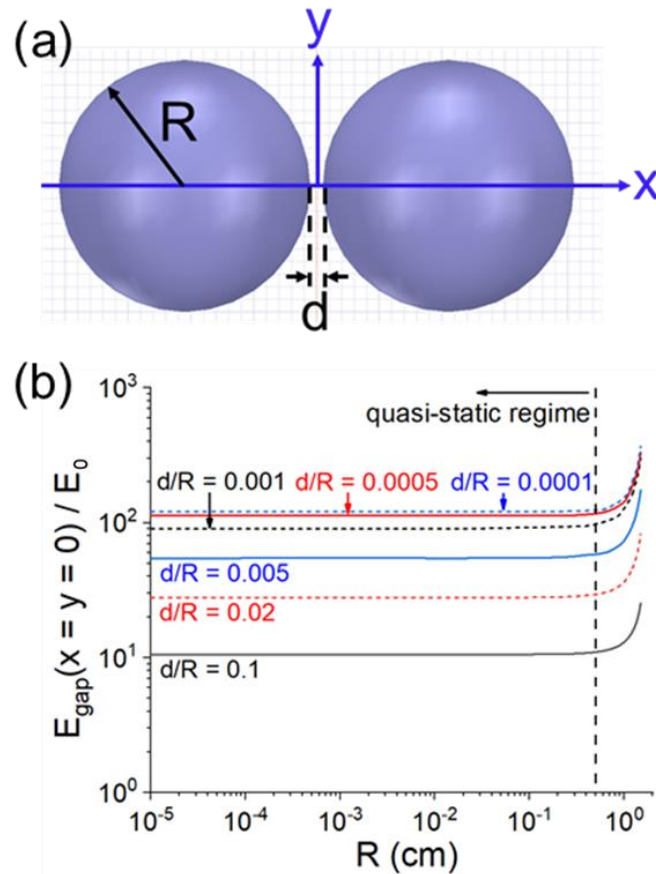
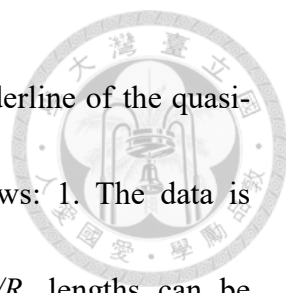


**Figure 4.2:** Validity check of the quasi-static regime. (a) A dimer formed of two identical dielectric spheres with  $\varepsilon/\varepsilon_0 = 20$ , separation  $d$  and radius  $R$  is located on the  $z = 0$  plane with the aligned direction along  $x$ -axis. A downward 2.45-GHz plane wave linearly polarized in the  $x$ -direction incidents on the dimer. (b)  $E_{\text{gap}}(x = y = 0)/E_0$  as functions of  $R$  for different values of  $d/R$ . Note that  $E_{\text{gap}}(x = y = 0)/E_0$  converges as  $d/R \rightarrow 0$ .





Almost all micro-sized particles for sintering is below the borderline of the quasi-static regime. In this regime, results can be generalized as follows: 1. The data is independent of frequency  $f$ . 2. For configurations with fixed  $d/R$ , lengths can be normalized to  $R$  and E-fields normalized to  $E_0$  and 3. The magnetic field, scattering, reflection (included in the simulation) are negligibly small. Beyond the quasi-static regime, the solution is complicated by electromagnetic resonances (see Chap. 3).

## 4.2 Electric Field Profiles in the Quasi-Static Regime

Figure 4.3(a) shows a representative E-field pattern in the quasi-static regime with the same model in Fig. 4.2(a). Figure 4.3(b) shows the  $E/E_0$  profiles along the  $x$ -axis for several  $d/R$ .  $E_{gap}(x, y=0)$ , the E-field along  $x$ -axis, is relatively constant in the gap, with a maximum of  $E_{gap}(x=y=0)/E_0 = 10.5, 28, \text{ and } 55$  for  $d/R = 0.1, 0.02, \text{ and } 0.005$ , respectively. On the other hand, profiles of the E-field along  $y$ -axis  $E_{gap}(x=0, y)$ , decreases sharply away from  $y=0$  with a HMHW value of  $0.35R, 0.17R, \text{ and } 0.10R$  for  $d/R = 0.1, 0.02, \text{ and } 0.005$ , respectively. Along both the  $x$ - and  $y$ -axes, the  $E_{gap}$  features a narrow spatial extent, an indication of the localized nature of E-field intensification in the gap region.

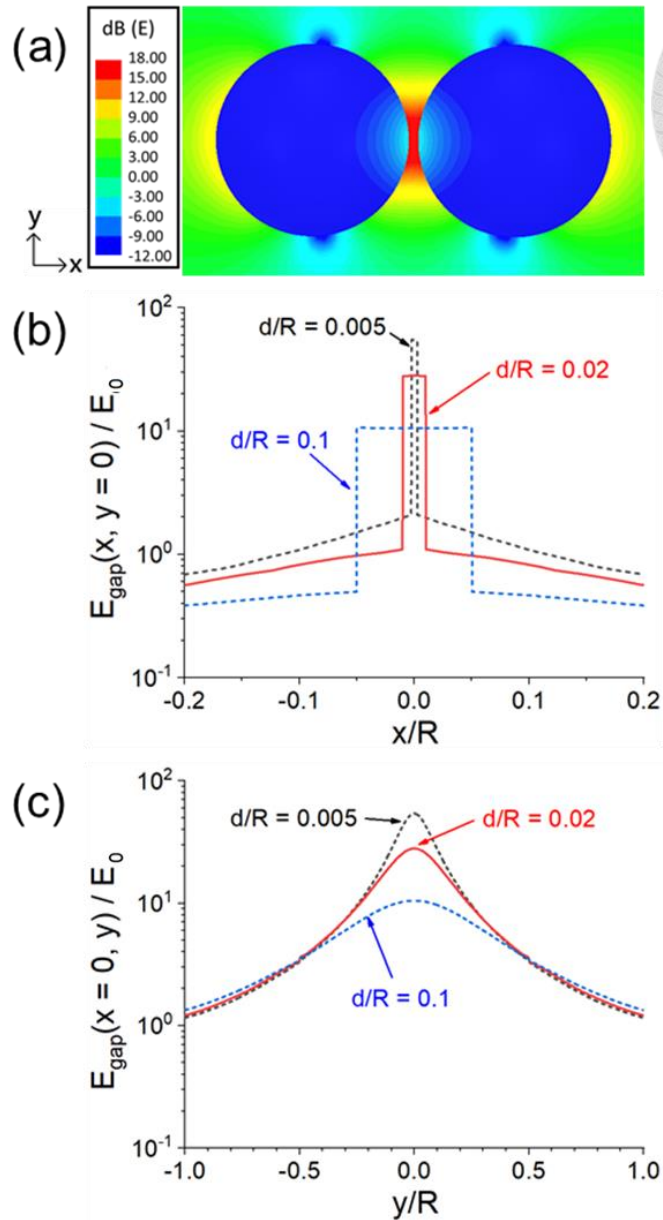


**Figure 4.3:** An illustration of the intensified  $E_{\text{gap}}$  between two closely spaced spheres with  $\varepsilon/\varepsilon_0 = 20$ , radius  $R$ , and variable separation  $d$ . The spheres are under a downward 2.45-GHz,  $x$ -polarized incident plane wave. (a) E-field pattern for  $d/R = 0.1$  on the  $x$ - $y$  plane through the centers of the two spheres. The color code gives the electric field (normalized to  $E_0$ ) in logarithmic scale. (b) Profiles of  $E_{\text{gap}}(x, y=0)/E_0$  along the  $x$ -axis for  $d/R = 0.005, 0.02$ , and  $0.1$ . (c) Profiles of  $E_{\text{gap}}(x=0, y)/E_0$  along the  $y$ -axis for  $d/R = 0.005, 0.02$ , and  $0.1$ .

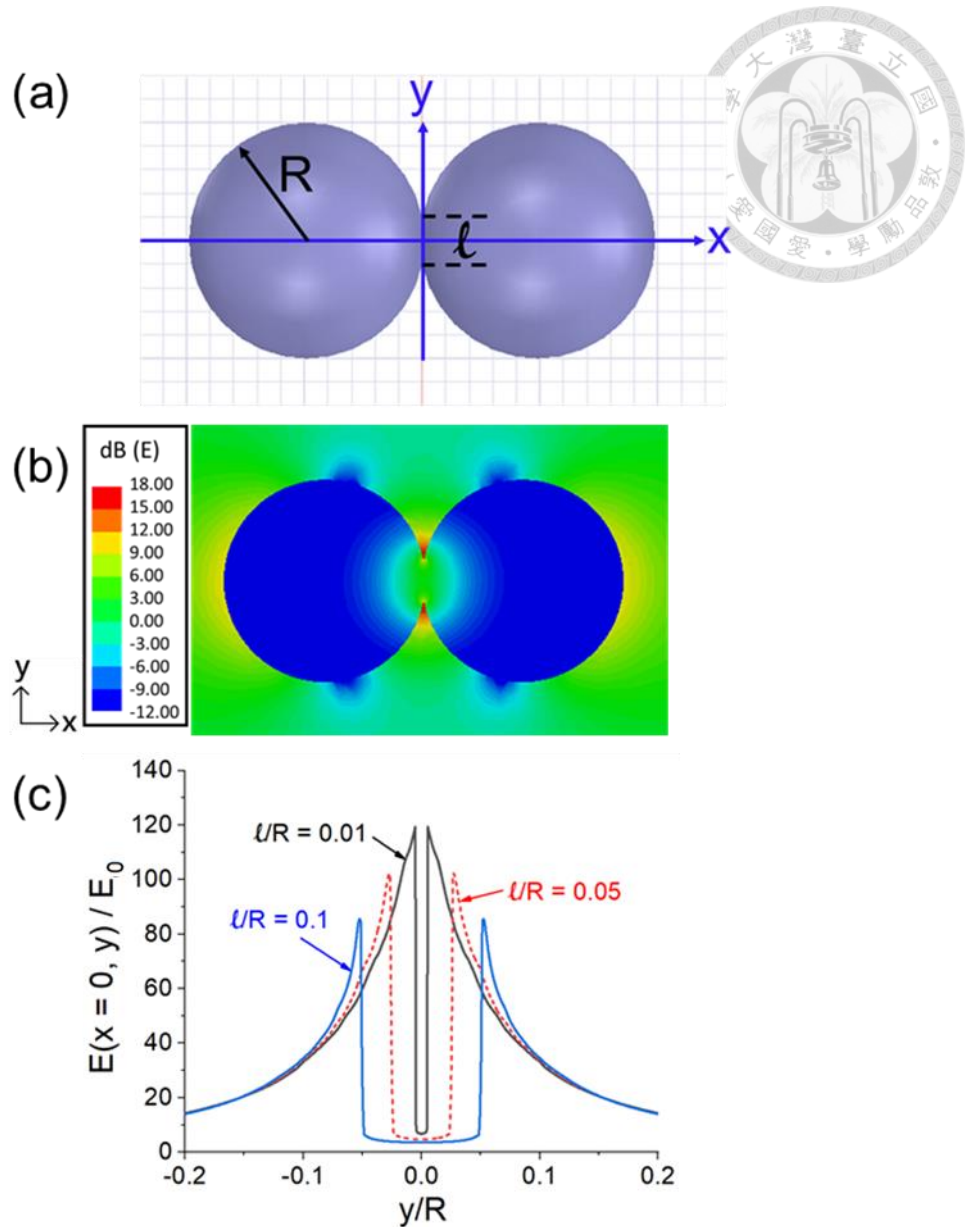


**Figure 4.4:** An illustration of intensified  $E_{gap}$  between two connected spheres. (a) Two dielectric spheres with  $\varepsilon/\varepsilon_0 = 20$  and radius  $R$  with a variable neck diameter  $l$  are exposed to a downward 2.45-GHz incident plane wave with  $E_0$  linearly polarized in the  $x$ -direction. (b) The E-field pattern for  $l/R = 0.4$  on the  $x$ - $y$  plane, which cuts through the centers (at  $z = 0$ ) of the two spheres. The color code gives  $\log_{10}(E/E_0)$ . (c) The  $E(x=0, y)/E_0$  profiles along the  $y$ -axis for  $l/R = 0.01, 0.05$ , and  $0.1$ .

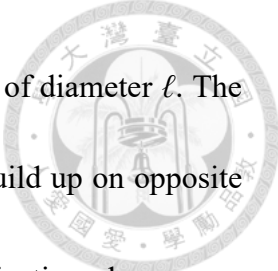
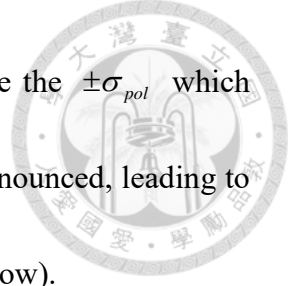


Figure 4.4(a) displays two spheres connected by a circular neck of diameter  $\ell$ . The surfaces are spherical up to the neck. In this case,  $\pm\sigma_{pol}$  can still build up on opposite sides of the gap around the neck. Without free electrons, the polarization charges are locked inside the molecules, fail to move and neutralize each other. Under the same radiation condition, Fig. 4.4(b) plots the E-field pattern for  $\ell/R = 0.4$ .  $E(x = 0, y)$ , the E-field profiles along the  $y$ -axis, is shown in Fig. 4.4(c) for several  $\ell/R$ . The maximum E-field is at the periphery of the neck ( $x = 0, y = \pm \ell/2$ ).

For both the connected and closely-spaced spheres, the significantly reduces with an increasing  $d/R$  or  $\ell/R$ . However, the reduction reasons are different.

For closely spaced spheres in Fig. 4.3, the exterior E-field  $E_0\mathbf{e}_x$  induces  $\pm\sigma_{pol}$  separately on the left and right half of each sphere. While the intensified  $E_{gap}$  is established by the mutually enhancement of inner-surface charges, the oppositely oriented  $\pm\sigma_{pol}$  on the outer surfaces produce a reverse E-field to partially cancel the  $E_{gap}$ . If the spheres remain enough close, the cancellation effect is negligibly minimal. On the contrary, the reduction of  $E_{gap}$  is significant for a larger  $d/R$ , with weaker enhancement of  $\pm\sigma_{pol}$  on the gap surfaces.

For the connected spheres, there are two different effects accounting for the  $E_{gap}$  reduction with  $\ell/R$ . First, a greater  $\ell/R$  means a shorter distance between the  $\pm\sigma_{pol}$  on the outer surfaces, resulting a more appreciable cancellation of the  $E_{gap}$ . Second, for a



larger  $\ell/R$ , there is less surface area across the gap to accommodate the  $\pm\sigma_{pol}$  which induces less  $E_{gap}$ . At a higher  $\varepsilon/\varepsilon_0$ , these two effects are more pronounced, leading to a more rapid drop of  $E_{gap}$  with  $\ell/R$  (as will be shown in Fig. 4.7 below).

### 4.3 Attractive Force Density on Spherical Surface

The highly intensified gap E-field between the strong  $\pm\sigma_{pol}$  suggests a considerable attractive force between the spheres. Because the force on each sphere is mirror-inversed, for simplification, only the left sphere is considered here. We use the  $x$ -axis (instead of the commonly used  $z$ -axis) as the zenith direction,  $r$  as the radial coordinate,  $\varphi$  as the azimuthal angle,  $\theta$  as the polar angle and the center of the left sphere as the origin of spherical coordinates [see Fig. 4.5(a)]. The quasi-static fields and electrical potential are independent of  $\varphi$  by symmetry; therefore,  $E_\varphi = 0$  and the  $\sigma_{pol}$  (at  $r = R$ ) depends only on  $\theta$ .

Because a charge is not influenced by its own field, the force per unit area on the sphere surface cannot be simply presented as  $\sigma_{pol}\mathbf{E}$ . Discounting the self-field, the effective E-field ( $E_{eff}$ ) experienced by  $\sigma_{pol}$  is the average E-fields on both sides of the  $r = R$  surface [109]:

$$\mathbf{E}_{eff}(R, \theta) = \frac{1}{2}[\mathbf{E}(R^-, \theta) + \mathbf{E}(R^+, \theta)] \quad (4.1)$$



where  $R^\pm = R \pm \delta$  with  $\delta \rightarrow 0$ . The self-field of  $\sigma_{pol}(R, \theta)$  is perpendicular to the surface; hence, only  $E_r(R^-, \theta)$  and  $E_r(R^+, \theta)$  are different while  $E_\theta$  is continuous across  $r = R$ . Thus,

$$\mathbf{E}_{eff}(R, \theta) = \frac{1}{2} [E_r(R^-, \theta) + E_r(R^+, \theta)] \mathbf{e}_r + E_\theta(R, \theta) \mathbf{e}_\theta \quad (4.2)$$

where  $\mathbf{e}_r$  is a unit vector along the radial coordinate. Without free charge, the perpendicular electrical displacement ( $D_r = \varepsilon_0 E_r$  in free space;  $D_r = \varepsilon E_r$  in the sphere) is always continuous, indicating a sharp discontinuity in  $E_r$  [e.g., Figure 4.3(c)]:

$$E_r(R^-, \theta) = E_r(R^+, \theta) \frac{\varepsilon_0}{\varepsilon} \quad (4.3)$$

Equations (4.2) and (4.3) give

$$\mathbf{E}_{eff}(R, \theta) = \frac{E_r(R^+, \theta)}{2} (1 + \frac{\varepsilon_0}{\varepsilon}) \mathbf{e}_r + E_\theta(R, \theta) \mathbf{e}_\theta \quad (4.4)$$

Applying the boundary condition on  $E_r$  (Gauss law) and using Eq. (4.3),

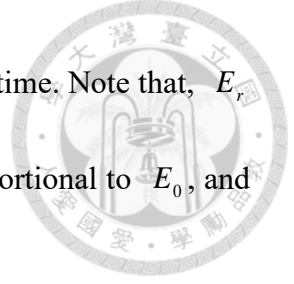
$$(1 - \frac{\varepsilon_0}{\varepsilon}) E_r(R^+, \theta) = \frac{\sigma_{pol}(R, \theta)}{\varepsilon_0}, \quad (4.5)$$

or

$$\sigma_{pol}(R, \theta) = \varepsilon_0 (1 - \frac{\varepsilon_0}{\varepsilon}) E_r(R^+, \theta) \quad (4.6)$$

$\sigma_{pol}$ ,  $E_r$ , and  $E_\theta$  all oscillate in phase in the quasi-static regime. So, the time-averaged force density (force per unit area) is

$$\begin{aligned} \langle \mathbf{f}(R, \theta) \rangle_t &= \langle \sigma_{pol}(R, \theta) \mathbf{E}_{eff} \rangle_t \\ &= \frac{1}{4} \varepsilon_0 (1 - \frac{\varepsilon_0^2}{\varepsilon^2}) E_r^{2,peak}(R^+, \theta) \mathbf{e}_r + \frac{1}{2} \varepsilon_0 (1 - \frac{\varepsilon_0}{\varepsilon}) E_r^{peak}(R^+, \theta) E_\theta^{peak}(R, \theta) \mathbf{e}_\theta \end{aligned} \quad (4.7)$$



where the superscript “peak” of a symbol indicates its peak value in time. Note that,  $E_r$  and  $E_\theta$  are derived under the quasi-static condition, hence are proportional to  $E_0$ , and depend only on the normalized  $d/R$  or  $\ell/R$ .

Let the  $r$  and  $\theta$ -components of the force density in Eq. (4.7) be  $\langle f_r(R, \theta) \rangle_t$  and  $\langle f_\theta(R, \theta) \rangle_t$ , respectively. With an incident field of  $E_0(\text{peak}) = 200 \text{ V/cm}$ , Fig. 4.5 shows the profiles of these two force densities as a function of  $\theta$  ( $0 < \theta < \pi$ ), where two spheres are closely spaced with  $d/R = 0.02$  and  $\varepsilon/\varepsilon_0 = 20$ . The force density is symmetric about the  $x$ -axis, with a sharp and narrow peak of  $\langle f_r(R, \theta) \rangle_t$  at  $\theta \approx 0$ . With same radiation condition, Fig. 4.6 shows the counterpart of Fig. 4.5, where two spheres are connected with permittivity  $\varepsilon/\varepsilon_0 = 20$  and  $\ell/R = 0.2$ . Because  $\theta_n$  is the polar angle of the periphery of the neck, there is no force for  $\theta < \theta_n$ . Similar to the results in Fig. 4.5, there is a sharp and narrow peak of  $\langle f_r(R, \theta) \rangle_t$  at  $\theta \approx \theta_n$ .

According to Figs. 4.5 and 4.6, the force density maximizes at  $\theta = 0$  for closely spaced spheres and at  $\theta_n$  for connected spheres. Denote these spatial maxima by  $\langle f(R, \theta = 0) \rangle_t$  and  $\langle f(R, \theta = \theta_n) \rangle_t$ . In Fig. 4.7(a) and (b), they are plotted in physical unit as continuous functions of  $d/R$  and  $\ell/R$ , for  $E_0(\text{peak}) = 200 \text{ V/cm}$  and  $\varepsilon/\varepsilon_0 = 5, 10$ , and 20. In both Figures 4.7(a) and (b), the force densities for  $\varepsilon/\varepsilon_0 = 20$  peak at  $\sim 130 \text{ dyne/cm}^2$ . The corresponding E-field is  $\sim 2.5 \times 10^4 \text{ V/cm}$ , slightly within the air breakdown strength of  $3 \times 10^4 \text{ V/cm}$  at 1 atm [63]. This is taken as the maximum force density without



air breakdown during the sintering processing. For lower values of  $\varepsilon/\varepsilon_0$ ,  $E_0(\text{peak})$  can be tuned upward to reach this maximum limitation.

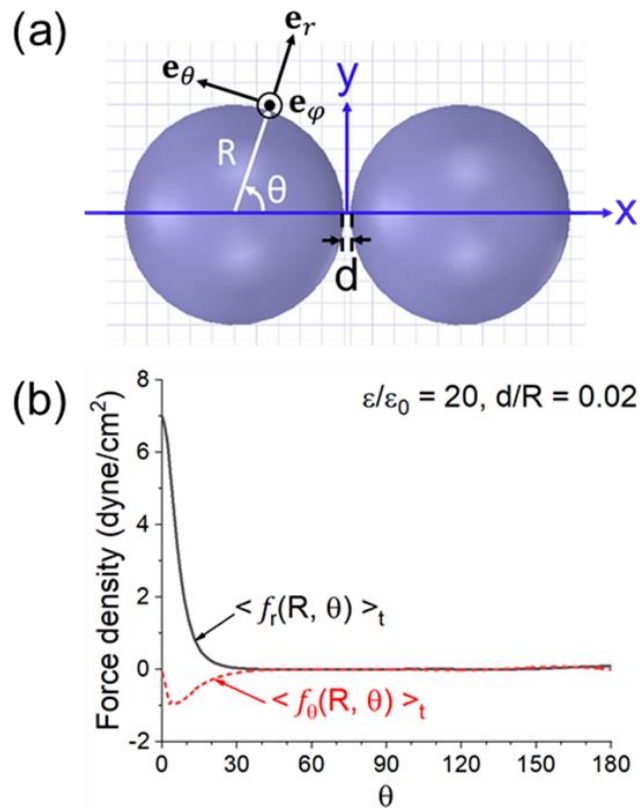


**Figure 4.5:** A sketch of the force density in physical unit for two closely spaced spheres with  $\varepsilon/\varepsilon_0 = 20$  and  $d/R = 0.02$  under  $E_0(\text{peak}) = 200$  V/cm. (a) Two closely spaced spheres on the  $x$ - $y$  plane. (b)  $\langle f_r(R, \theta) \rangle_t$  and  $\langle f_\theta(R, \theta) \rangle_t$  on the left sphere versus  $\theta$ .



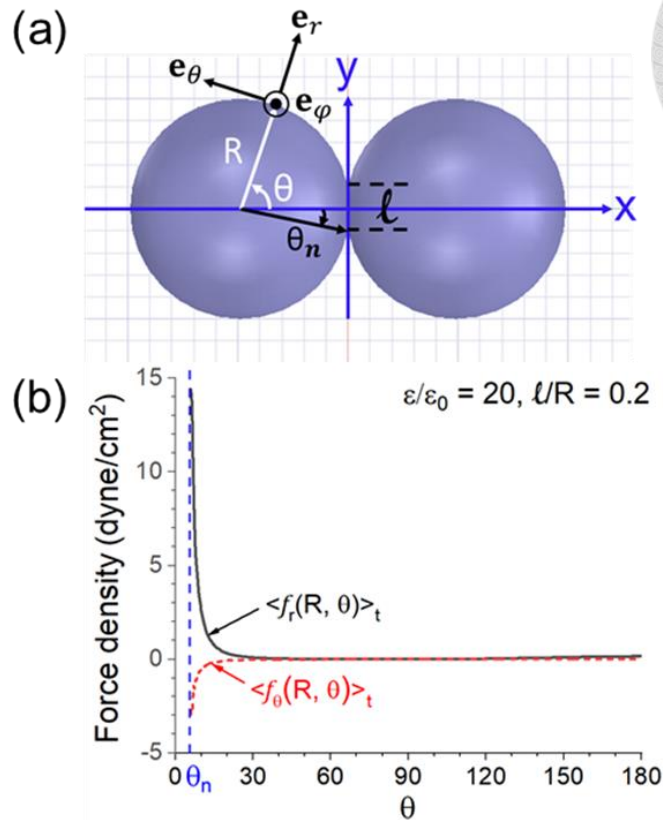


**Figure 4.6:** A sketch of the force density in physical unit for two connected spheres with  $\epsilon/\epsilon_0 = 20$  and  $l/R = 0.2$  under  $E_0(\text{peak}) = 200$  V/cm. (a) Two connected spheres with a neck diameter  $l/R$  plotted on the  $x$ - $y$  plane. (b)  $\langle f_r(R, \theta) \rangle_t$  and  $\langle f_\theta(R, \theta) \rangle_t$  versus  $\theta$ .

Because of the finite mesh size in simulation is finite, the smallest calculated  $d/R$  or  $l/R$  in Fig. 4.7 is  $10^{-4}$  (instead of 0), for which the force density reaches an absolute maximum. For both  $d/R \rightarrow 0$  and  $l/R \rightarrow 0$ , the absolute maxima converge to the same value, indicating a continuous transition from separation to connection. The force density covers a broad range in the parameter space. It decreases sharply with a greater  $d/R$  or  $l/R$ .

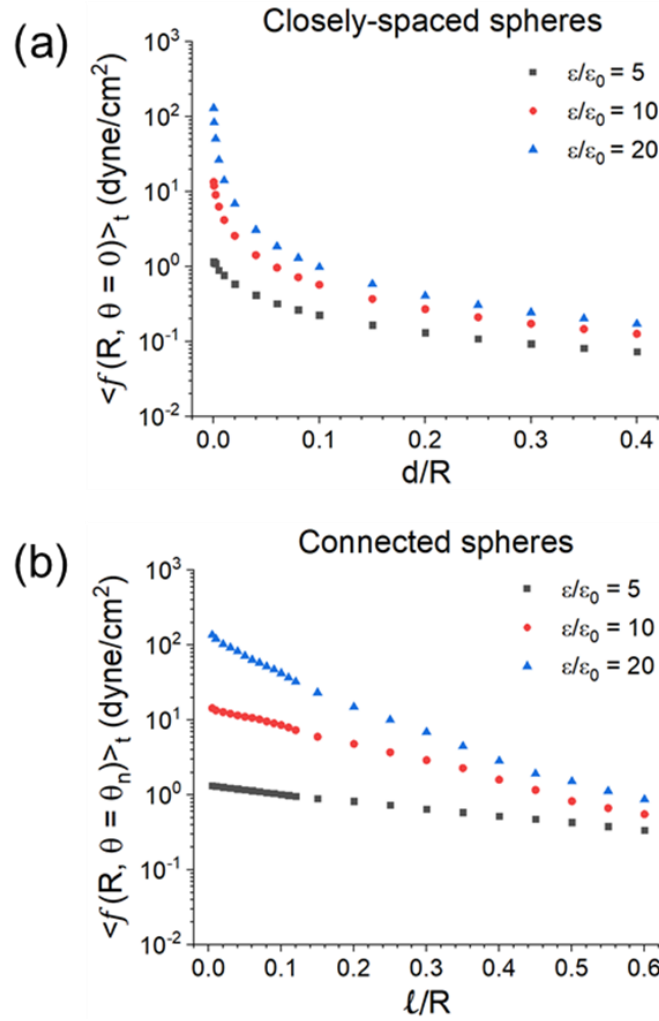


**Figure 4.7:** The maximum force density (with respect to  $\theta$ ) in physical unit for  $\epsilon/\epsilon_0 = 5, 10,$  and  $20$  under  $E_0(\text{peak}) = 200 \text{ V/cm}$ . (a)  $\langle f(R, \theta = 0) \rangle_t$  versus  $d/R$  for two closely spaced spheres. (b)  $\langle f(R, \theta = \theta_n) \rangle_t$  versus  $\ell/R$  for two connected spheres.

For the reasons discussed in connection with Fig. 4.4, the force density for two connected spheres decreases more rapidly with a larger  $\epsilon/\epsilon_0$ . Nevertheless, the lower ranges of  $d/R$  and  $\ell/R$  (where the force densities approach the highest values) are regions of interest to sintering (e.g., powder compaction and neck growth).



#### 4.4 Total Attractive Force between Two Spheres

By symmetry, the total attractive force between two closely-spaced spheres in the quasi-static regime is in the  $x$ -direction, given by

$$\begin{aligned} \langle f_x(R, \theta) \rangle_t &= \langle \mathbf{f}(R, \theta) \rangle_t \cdot \mathbf{e}_x \\ &= \frac{1}{4} \varepsilon_0 \left(1 - \frac{\varepsilon_0^2}{\varepsilon^2}\right) E_r^{2, peak}(R^+, \theta) \cos \theta - \frac{1}{2} \varepsilon_0 \left(1 - \frac{\varepsilon_0}{\varepsilon}\right) E_r^{peak}(R^+, \theta) E_\theta^{peak}(R, \theta) \sin \theta \end{aligned} \quad (4.8)$$

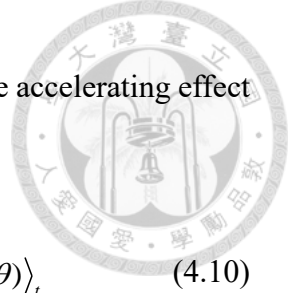
A surface integral then gives the total attractive force

$$\langle F_x(R, \theta) \rangle_t = \oint_s \langle f_x(R, \theta) \rangle_t da = 2\pi R^2 \int_0^\pi \langle f_x(R, \theta) \rangle_t \sin \theta d\theta \quad (4.9)$$

where  $da$  is a differential surface area. When the incident wave is polarized in the  $x$ -direction, the  $E_{gap}$  is at its maximum. Parallel to the sphere-assigned axis, it is the best direction for polarization-charge enhancement across the gap [61]. If the exterior E-field  $E_0$  is randomly polarized (e.g., in a microwave oven), the average force is isotropic with half of the value in Eqs. (4.7)-(4.9).

Fig. 4.5 shows the force density peaks at  $\theta \approx 0$  and is predominantly a radial force in the outward direction. It is proportional to the square of  $E_r$ , hence always attractive independent of the direction of the exterior E-field.

Because surface area is proportional to  $R^2$ , the total force of a micro-sized sphere is extremely small. In contrast, the total mass of the sphere is proportional to  $R^3$ . To sum up, smaller the sphere is, greater acceleration can be induced by the attractive force. In



terms of the accelerating effect, a useful figure of merit to quantify the accelerating effect

is the force on a unit volume of the sphere defined as

$$\frac{\text{force}}{\text{unit volume}} = \frac{\text{total force on sphere}}{\text{volume of sphere}} = \frac{3}{4\pi R^3} \langle F_x(R, \theta) \rangle_t \quad (4.10)$$

With the same radiation condition in Fig. 4.7, Fig. 4.8 shows the attractive force per unit volume as a function of  $R$  for two closely spaced spheres with different values of  $d/R$  and  $\epsilon/\epsilon_0$ . As in Fig. 4.7, all E-fields do not exceed the air breakdown strength at 1 atm. Consider the example of two closely-spaced spheres with  $\epsilon/\epsilon_0 = 20$ ,  $R = 1 \mu\text{m}$ , and  $d/R = 0.001$ . The attractive force per unit volume is  $\sim 5 \times 10^3 \text{ dyne/cm}^3$ . With a supposed specific weight of 2.5, the spheres will each have a frictionless acceleration of  $2 \times 10^3 \text{ cm/sec}^2$ , about twice the value of gravitational acceleration. For smaller spheres, this acceleration can be much greater. Under less favorable conditions, greater acceleration can be achieved by applying a larger  $E_0$ . The significance of this force will be discussed in next section.

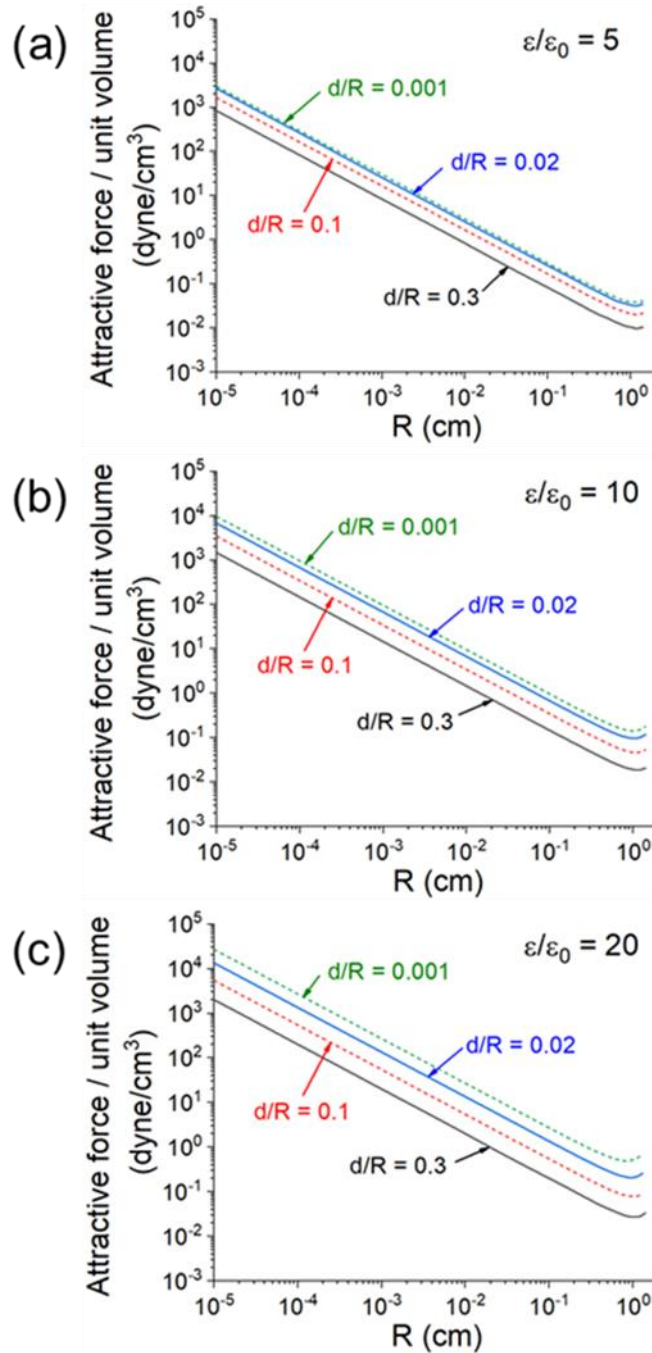
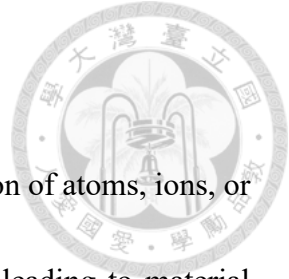


**Figure 4.8:** Attractive force per unit volume on each of two closely spaced spheres shown in Fig. 4.5(a) as a function of  $R$  for  $E_0$  (peak) = 200 V/cm and several values of  $d/R$ . (a)  $\epsilon/\epsilon_0 = 5$ , (b)  $\epsilon/\epsilon_0 = 10$ , and (c)  $\epsilon/\epsilon_0 = 20$ . For  $R > 0.5$  cm, fields are no longer quasi-static and electromagnetic resonances take place in the spheres.



## 4.5 Potential Significance to Microwave Sintering

As the detail discussion in Ref. [72], thermally activated diffusion of atoms, ions, or molecules is the primary process for matter transport in sintering, leading to material bonding and neck formation. In this process, there are a variety of paths involved, such as lattice, grain boundary, and surface diffusion. Several nonthermal effects are proposed in previous sections to interpret the lower temperature requirement in microwave sintering. In this section, we further argue on the viability of the electric force as a nonthermal effect.

In Sec. 4.3, the electric force between two neighboring dielectric spheres is always attractive. It is a microscopic, non-contact force far different from the contact force due to an externally applied pressure. In the beginning stage of sintering, the sample is usually a compacted mass of spherical particles. Assume two closely-spaced,  $R = 1 \mu\text{m}$  particles with 2.5 in specific weight, are irradiated by an exterior microwave with  $E_0(\text{peak}) = 200 \text{ V/cm}$  (typical of a household microwave oven). According to Fig. 4.8, the particles will each experience a frictionless acceleration up to several  $g$  ( $= 980 \text{ cm/sec}^2$ ) without an air breakdown. This is expected to assist the powder compaction in a significant manner, as compared to the methods of gravitational or centrifugal settling [72].

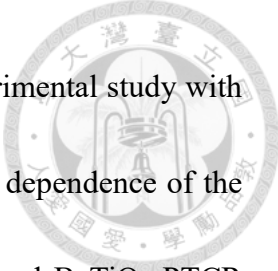
During the formation and growth of an inter-particle neck, the force will continue to shift to the gap around the newly formed neck. Just below the air breakdown, this force

can exceed 100 dyne/cm<sup>2</sup> [Fig. 4.7(b)]. Its persistent presence is expected to play an important role in the neck growth, especially in the liquid phase.



Liquid-phase sintering can occur below the melting temperature of the major sample under treatment. Mixing with a small quantity of additives, the inadequate densification problem of the major component can be remedied. The commonly used additives (SiO<sub>2</sub>, CaO, MgO, SrO, BaO, La<sub>2</sub>O<sub>3</sub>, Y<sub>2</sub>O<sub>3</sub>, and TiO<sub>2</sub>) have a dielectric constant of 2 (SiO<sub>2</sub>) to 60 (TiO<sub>2</sub>) [110]. Surface melting of major particles often significantly enhance the mass transport. For example, densification of ~1% La<sub>2</sub>O<sub>3</sub>/BaO-doped ZST ceramic can be completed at 1350°C, which is about 275°C lower than the un-doped case [111]. In fact, as stated in a recent review [79], the liquid phase exists in over 70% formation of all sintered products. For commercial sintered products, the proportion is about 90%.

The reduction in free energy of the consolidated system is main driving force in sintering processing [72]. This is usually accomplished by atomic diffusion which causes body densification by matter transport into the pores. Similar considerations suggest the tendency of surface bonding by the attractive force across a high  $E_{gap}$  [Fig. 4.7(b)], thereby releasing the E-field energy. The neck growth may also be facilitated by surface tension, which can lead to a reduction of the surface area, hence a lower surface energy state.



Notably, the current theory is highly correlated to an early experimental study with orientational effects. Chang' crew found a significantly orientational dependence of the sample shrinkage rates and grain growth in sintering process of doped BaTiO<sub>3</sub> PTCR materials which is heated to 1250°C by a linearly polarized microwave [112]. Parallel to the direction of exterior E-field, the shrinkage comes to maximum with magnitude 48%. In comparison, the perpendicular-direction shrinkage is only 26%. The sintered grains also show a strip like microstructure oriented along the E-field. The authors gave no clear reasons for this phenomenon. Nevertheless, the directional coincidence between this phenomenon and maximum polarization-charge buildup suggests the attractive force as a plausible cause. To draw a definitive conclusion, more experimental evidence is apparently needed due to the complexity of the sintering process.



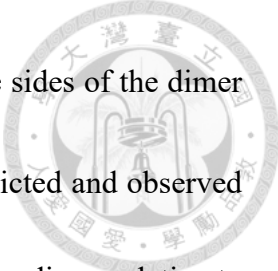
## CONCLUSION



After decades of research, the field of microwave is still under active investigation both academically and in industrial applications. Along with new areas of research, such as chemical analysis, ceramic sintering and popular science in social media, more and more questions arise, which call for deep physical insights for their explanations.

In Chap. 1, the relevant microwave physics is reviewed and the quasi-static regime is defined. In Chap. 2, microwave behavior in dielectrics under an incident plane wave is investigated. At low wave frequencies, the irradiated target is in the quasi-static regime. Although the penetration depth is longer than the spatial scale, the polarization charge shields a large amount of exterior electric field from entering the target. In combination with a low power absorption rate, microwave heating at low frequency is inefficiency in general. On the other hand, the high frequency features a shallower penetration depth. However, considering electromagnetic resonances, the field penetrates deeper into the target. This results in a high power absorption rate to allow targets with large spatial scales to be significantly heated. By choosing reasonable frequency, microwave heating rate and heating uniformity can be both optimized.

A new explanation is given to a household puzzle in social media in Chap. 3. At 27 MHz, a dominantly electrical environment, sparks in aqueous dimers are predicted and observed, which proves the electrical origin for the phenomenon. Specifically, a buildup



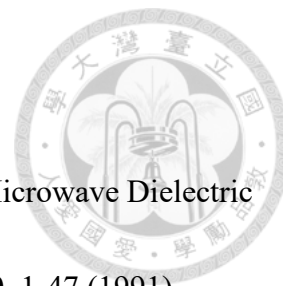
of  $\pm\rho_{gap}$ , hence the E-field, by 2–3 orders-of-magnitude on opposite sides of the dimer gap causes the air arcing. This is supported by the agreement of predicted and observed threshold conditions. The absence of sparks upon a  $90^\circ$  rotation of the dimer relative to exterior E-field  $E_0$  provides additional evidence. Further simulations over a broad frequency range indicate the viability of the electrical origin even in the presence of the first few electromagnetic resonances in the dimer. In particular, gap arcing and sphere attraction at 2.45 GHz were experimentally demonstrated. These results shed new light into the basic properties of isolated dimers. It may hopefully be a useful reference for the investigation of the electromagnetic behavior of complex systems.

Chapter 4 presents a detailed theory on the electric attractive force between the two dielectric spheres of a dimer due to microwave radiation. This force is significant in that (1) It is an inherent inter-particle force in microwave sintering of powder compacts; (2) It concentrates in regions (gap surfaces between two sintering particles nearly in touch or connected by a neck) where the primary sintering process takes place; and (3) It has a significant strength to play a supplemental role in particle bonding and neck growth normally achieved by thermally activated atomic diffusion. Microwave sintering is a method known to require a substantially lower processing temperature than conventional sintering for reasons still under investigation. The attractive force therefore offers a plausible explanation. For example, its orientation along the E-field is consistent with an

early sintering experiment, which found much greater sample shrinkage and a strip-like microstructure in the direction of the wave E-field. Hopefully, the formalism and data base presented here could be a useful reference for a more definitive investigation.



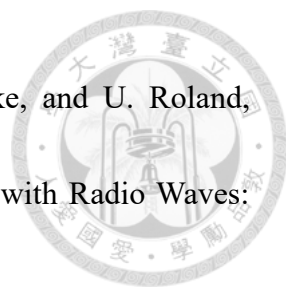
## REFERENCE



- [1] D. Michael, P. Mingos, and D. R. Baghurst, "Applications of Microwave Dielectric Heating Effects to Synthetic in Chemistry," *Chem. Soc. Rev.* **20**, 1-47 (1991).
- [2] J. T. Senise and L. A. Jermolovicius, "Microwave Chemistry – A Fertile Field for Scientific Research and Industrial Application," *Journal of Microwaves and Optoelectronics* **3** (2004).
- [3] A. de la Hoz, A. Diaz-Ortiz, and A. Moreno, "Microwaves in Organic Synthesis. Thermal and Non-thermal Microwave Effects," *Chem. Soc. Rev.* **34**, 164-178 (2005).
- [4] D. Gangrade, S. D. Lad, and A. L. Mehta, "Overview on Microwave Synthesis – Important Tool for Green Chemistry," *Int. J. Res. Pharm. Sci.* **5**(2), 37-42, 2015
- [5] Yunshen Zhang, "The Application of Microwave Technology in Chemistry and Chemical Engineering", *Iconf-EM 2016*, 2352-5428 (2017).
- [6] S. Marinel, et al., "Microwave Sintering of Alumina at 915 MHz Modeling, Process Control, and Microstructure Distribution," *Materials (Basel)* **12**(16), 2544 (2019)
- [7] Di Zhai, et al., "Microwave transmission performance of fused silica ceramics in microwave high-temperature heating," *Ceramics International* **45**(5), 6157-6162 (2019).
- [8] Qi Liang, et al., "Large Area Single-Crystal Diamond Synthesis by 915 MHz




- Microwave Plasma-Assisted Chemical Vapor Deposition,” *Cryst. Growth Des.* **14**(7), 3234-3238 (2014).
- [9] D. Guan, M. Cheng, Y. Wang, and J. Tang, “Dielectric Properties of Mashed Potatoes Relevant to Microwave and Radio-frequency Pasteurization and Sterilization Processes,” *Journal of Food Science* **69** (2004).
- [10] S. P. Singh, “An Analysis of Dielectric Parameters and Parameters and Penetration Depth of Tomato Sauces,” *J. Food Process. Technol.* (2018).
- [11] M. S. Venkatesh, and G. S. V. Rahavan, “An Overview of Microwave Processing and Dielectric Properties of Agri-food Materials,” *Biosystems Engineering* **88**(1), 1-18 (2004).
- [12] Qiushan Guo, Da-Wen Sun, Jun-Hu Cheng, Zhong Han, “Microwave processing techniques and their recent applications in the food industry,” *Trends in Food Science & Technology* **67**, 236-247 (2017).
- [13] Deandrae L. Smith, et al., “Implications of microwave drying using 915 MHz frequency on rice physicochemical properties,” *Cereal Chemistry* **95**(2), 211-225 (2017).
- [14] S. O. Nelson, “Review and Assessment of Radio-frequency and Microwave Energy for Stored-grain Insect Control,” *Transactions of the A.S.A.E.* **39**(4), 1475-1484 (1996).

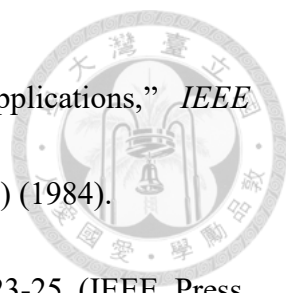
- 
- [15] M. Kraus, F. Holzer, C. Hoyer, U. Trommler, F.-D. Kopinke, and U. Roland, “Chemical-free Pest Control by Means of Dielectric Heating with Radio Waves: Selective Heating,” *Chem. Eng. Technol.* **41**, 116-123 (2018).
- [16] Ioan Valentin Moise, Mihaela Ene, Constantin Daniel Negut, Mihalis Cutrubinis, and Maria Mihaela Manea, “Radiation processing for cultural heritage preservation – Romanian experience,” *Nukleonika* **62**(4), 253-260 (2017).
- [17] Bruno Bisceglia, Roberto De Leo, Anna Pia Pastore, Svetlana von Gratowski, and Viatcheslav Meriakri, “Innovative Systems for Cultural Heritage Conservation. Millimeter Wave Application for Non-invasive Monitoring and Treatment of Works of Art,” *Journal of Microwave Power and Electromagnetic Energy* **45**(1), 36-48 (2011).
- [18] Roberto Bacchiani, Bruno Bisceglia, and Roberto De Leo, “Industrial Applications of Microwaves: Cultural Heritage Conservation,” *Interazioni fra Campi Elettromagnetici e Biosistemi* 27-29 (2012).
- [19] T. Cerchiara, A. M. Palermo, G. Esposito, and G. Chidichimo, “Effects of microwave heating for the conservation of paper artworks contaminated with *Aspergillus versicolor*,” *Cellulose* **25**, 2063–2074 (2018).
- [20] L. Capineri, L., et al. “Microwave reflectometry for the diagnostic of cultural heritage assets,” *PIERS Proceedings*, Kuala Lumpur, Malaysia, 778–781 (2012).



- [21] F. Cappitelli, C. Cattò, F. Villa, “The Control of Cultural Heritage Microbial Deterioration,” *Microorganisms* **8**, 1542 (2020).
- [22] R. Pierdicca, et al., “Accurate Modeling of the Microwave Treatment of Works of Art,” *Sustainability* **11**, 1606 (2019).
- [23] C. Crova, F. Chiadini, L. Di Maio, L. Guerriero, L. Pescione, “Elimination of Xylophages from Wood through Microwave Treatment: Microstructural Experiments,” *Conserv. Sci. Cult. Herit.* **17**, 45–57 (2018).
- [24] S. O. Nelson, P. G. Bartley, K. C. Lawrence, “RF and microwave dielectric properties of stored-grain insects and their implications for potential insect control,” *Transactions of the ASAE.* **41**(3), 685-692 (1998).
- [25] Bruno Bisceglia, et al. “MW treatment of wooden handicrafts. The restoration of San Leone Magno statue,” in 30th Bioelectromagnetics Society Annual Meeting, 8-12 (2008).
- [26] Anna Pia Pastore, et al, “An innovative microwave system for wooden art object disinfestation,” *International Journal of Computations and Mathematics in Electrical* **31**(4), 1173-1177 (2012).
- [27] Bisceglia Bruno, et al., “Innovative Systems for Cultural Heritage Conservation. Millimeter Wave Application for Non-invasive Monitoring and Treatment of Works of Art,” *J Microw Power Electromagn Energy* **45**(1), 36-48 (2011).

- 
- [28] V. Vivancos-Ramón, et al., “Microwave treatment for woodworm disinfection in large-format works of art,” *International Microwave Power Institute* (2006).
- [29] Antonella Altieri, et al., “Non invasive treatment of works of art. Application of MMW and THz radiations for diagnostics and disinfestations,” in 32th Bioelectromagnetics Society Annual Meeting (2010).
- [30] Andrea Doria, et al., “An Alternative Phase-Sensitive THz Imaging Technique for Art Conservation: History and New Developments at the ENEA Center of Frascati,” *Appl. Sci.* **10**(21), 7661 (2020).
- [31] Myung-Heui Woo, Adam Grippin, Chang-Yu Wu, Joseph Wander, “Microwave-irradiation-assisted HVAC Filtration for Inactivation of Viral Aerosols,” *Aerosol and Air Quality Research* **12**, 295–303 (2012).
- [32] Ma Ai-yuan, Zheng Xue-mei, Peng Jin-hui, “Dechlorination of zinc oxide dust derived from zinc leaching residue by microwave roasting in a rotary kiln,” *Brazilian Journal of Chemical Engineering* **34**(1), 193-202 (2017).
- [33] Can Wang, Xurui Hu, Zhiwei Zhang, “Airborne disinfection using microwave-based technology Energy efficient and distinct inactivation mechanism compared with waterborne disinfection,” *Journal of Aerosol Science* **137** (2019).
- [34] Yang Lv, et al., “Study on microwave sterilization technology of humidifier in central air-conditioning system,” *Building and Environment* **160** (2019).



- 
- [35] J. M. Osepchuk, “A History of Microwave Heating Applications,” *IEEE Transactions on Microwave Theory and Techniques* **MTT-32**(9) (1984).
- [36] R. F. Harrington, *Time-Harmonic Electromagnetic Fields*, 23-25 (IEEE Press, 2001).
- [37] P. J. W. Debye, *Polar Molecules* (Chemical Catalog Co., New York, 1929).
- [38] U. Kaatze, “Complex permittivity of water as a function of frequency and temperature,” *J. Chem. Eng. Data* **34**, 371–374 (1989).
- [39] S. O. Nelson, and A. W. Kraszewski, “Dielectric Properties of Materials and Measurement Techniques,” in *Drying Technology*, Marcel Dekker, Inc., 1123-1142 (1990).
- [40] J. D. Jackson, *Classical Electrodynamics*, 3rd ed. (John Wiley, New York, 1998).
- [41] D. K. Cheng, *Field and Wave Electromagnetics*, 2nd ed. (Addison-Wesley Publishing Company, 1989).
- [42] R. Feynman, *The Feynman Lectures on Physics*, Volume II (Addison-Wesley Publishing Company, 2006).
- [43] Kuan-Wen Chen, “An Investigation on Microwave Dielectric Heating: Polarization Charge Shielding Effect and Microwave Resonance Phenomenon,” master thesis, National Taiwan University, Taiwan (2019).
- [44] R. F. Harrington, *Time-Harmonic Electromagnetic Fields*, Chapter 5 & 6 (IEEE



Press, 2001).

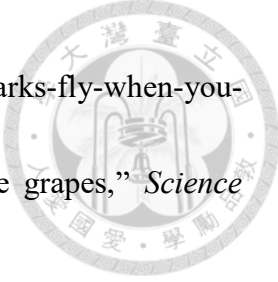
- [45] P. Chow, "An Analytical Study on the Boundary Value Problem for Wave Propagation along a Circular Cylinder," master thesis, National Taiwan University, Taiwan, (2018).
- [46] J. A. Stratton, *Electromagnetic Theory*, 406-414, (McGraw-Hill Book Company, Inc., New York, 1941).
- [47] *Microwaves in Organic Synthesis*, 2nd ed., edited by A. Loupy (Wiley-VCH, Weinheim, Germany, 2006).
- [48] C. O. Kappe, "Microwave dielectric heating in synthetic organic chemistry," *Chem. Soc. Rev.* **37**, 1127-1139 (2008).
- [49] C. O. Kappe, A. Stadler, and D. Dallinger, *Microwaves in Organic and Medicinal Chemistry*, 2nd ed. (Wiley-VCH, Weinheim, Germany, 2012).
- [50] M. Charde, A. Shukla, V. Bukhariya, J. Mehta, and R. Chakole, "A review on significance of microwave assist technique in green technology," *International Journal of Phytopharmacy* **2**, 39-50 (2012).
- [51] C. Gabriel, S. Gabriel, E. H. Grant, B. S. J. Halstead, and D. M. P. Mingos, "Dielectric parameters relevant to microwave dielectric heating," *Chem. Soc. Rev.* **27**, 213-223 (1998).
- [52] P. Ratanadecho, K. Aoki, and M. Akahori, "A numerical and experimental





investigation of the modeling of microwave heating for liquid layers using a rectangular waveguide (effects of natural convection and dielectric properties),”


*Appl. Math. Modelling* **26**, 449-472 (2002).

- [53] W. Cha-um, P. Rattanadecho, and W. Pakdee, “Experimental and numerical analysis of microwave heating of water and oil using a rectangular waveguide: Influence of sample sizes, positions, and microwave power,” *Food Bioprocess Technology* **4**, 544-558 (2011).
- [54] T. Yousefi, S. A. Mousavi, M. Z. Saghir, and B. Farahbakhsh, “An investigation on the microwave heating of flowing water: A numerical study,” *International Journal of Thermal Sciences* **71**, 118-127 (2013).
- [55] S. P. Yeong, M. C. Law, C. C. V. Lee, and Y. S. Chan, “Modelling batch microwave heating of water,” *IOP Conf. Ser.: Mater. Sci. Eng.* **217**, 012035 (2017).
- [56] H. K. Khattak, P. Bianucci, and A. D. Slepko, “Linking plasma formation in grapes to microwave resonances of aqueous dimers,” *Proc. Natl. Acad. Sci. U.S.A.* **116**, 4000–4005 (2019).
- [57] R. Bansal, “The wrath of grapes?,” *IEEE Microwave Mag.* **20**, 11–12 (2019).
- [58] Research Highlight. “Why microwaving a grape sparks a fiery glow,” *Nature* **566**, 429 (2019).

- 
- [59] A. Fox, <https://www.sciencemag.org/news/2019/02/why-sparks-fly-when-you-microwave-grapes> for “Why sparks fly when you microwave grapes,” *Science Online* (2019).
- [60] A. Slepko, “Fruit photonics and the shape of water,” *Phys. Today* **73**(6), 62–63 (2020).
- [61] M. S. Lin, L. C. Liu, L. R. Barnett, Y. F. Tsai, and K. R. Chu, “On electromagnetic wave ignited sparks in aqueous dimers,” *Physics of Plasmas* **28**, 102102 (2021).
- [62] J. Monteiro, L. C. Costa, M. A. Valente, T. Santos, and J. Sousa, “Simulating the electromagnetic field in microwave ovens,” in SBMO/IEEE MTT-S International Microwave and Optoelectronics Conference (IMOC 2011), Natal., 493–497 (2011).
- [63] D. Halliday, J. Walker, and R. Resnick, *Fundamentals of Physics*, 10 ed., Chap. 25 (Wiley, Hoboken, NJ, 2014).
- [64] L. C. Liu, <https://youtube.com/watch?v=vLQkaxYTtVU&si=EnSIkaIECMiOmarE> for “Real-time sparks between two  $R = 7$  mm hydrogel spheres with 0.2 mm gap in a 27 MHz capacitor,” *YouTube* (2021).
- [65] L. C. Liu, <https://youtube.com/watch?v=e7xt6JJceM&si=EnSIkaIECMiOmarE> for “Real-time sparks between two  $R = 7$  mm hydrogel spheres with 0 gap in a 27 MHz capacitor,” *YouTube* (2021).

- 
- [66] L. C. Liu, [https://youtube.com/watch?v=ACWP9\\_vc2aY&si=EnSikaIECMiOma-rE](https://youtube.com/watch?v=ACWP9_vc2aY&si=EnSikaIECMiOma-rE) for “Real-time attraction between two  $R = 10$  mm spheres on a flat surface,  $d = 1.5$  mm and  $f = 2.45$  GHz,” *YouTube* (2021).
- [67] A. Birnboim, J. P. Calame, and Y. Carmel, “Microfocusing and polarization effects in spherical neck ceramic microstructures during microwave processing,” *J. Appl. Phys.* **85**, 478–482 (1999).
- [68] S. Horikoshi, A. Osawa, S. Sakamoto, and N. Serpone, “Control of microwave-generated hot spots. Part V. Mechanisms of hot-spot generation and aggregation of catalyst in a microwave-assisted reaction in toluene catalyzed by PD-loaded AC particulates,” *Appl. Catal. A* **460–461**, 52–60 (2013).
- [69] X. Qiao and X. Xie, “The effect of electric field intensification at interparticle contacts in microwave sintering,” *Sci. Rep.* **6**, 32163 (2016).
- [70] N. Haneishi, S. Tsubaki, E. Abe, M. M. Maitani, E. Suzuki, S. Fujii, J. Fukushima, H. Takizawa, and Y. Wada, “Enhancement of fixed-bed flow reactions under microwave irradiation by local heating at the vicinal contact points of catalyst particles,” *Sci. Rep.* **9**, 222 (2019).
- [71] M. Liu, L. Zhang, W. Zhou, J. Gao, P. Wang, and G. Zhao, “The mechanism of microwave-induced discharge between submillimeter active coke,” *Plasma Sources Sci. Technol.* **29**, 075015 (2020).

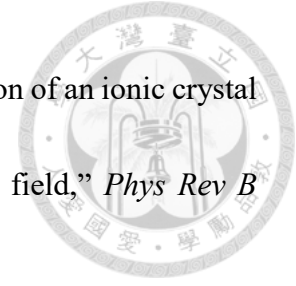
- 
- [72] M. N. Rahaman, *Ceramic Processing and Sintering*, 2nd ed. (Taylor & Francis Group, New York, 2017).
- [73] J. D. Katz “Microwave sintering of ceramics,” *Annu Rev Mater Sci* **22**, 153-170 (1992).
- [74] D. E. Clark, W. H. Sutton, “Microwave processing of materials,” *Annu Rev Mater Sci* **26**, 299-331 (1996).
- [75] M. Oghbaei, O. Mirzaee, “Microwave versus conventional sintering: A review of fundamentals, advantages and applications,” *J Alloys Compd* **494**, 175-189 (2010).
- [76] Z. Z. Fang, *Sintering of advanced materials*, 1<sup>st</sup> ed. (Woodhead Publishing Limited, Sawston, England, 2010).
- [77] K. I. Rybakov, E. A. Olevsky, E. V. Krikun, “Microwave sintering: fundamentals and modeling,” *J Am Ceram Soc* **96**(4), 1003-1020 (2013).
- [78] M. Bhattacharya, T. Basak, “Susceptor-assisted enhanced microwave processing of ceramics - a review,” *Crit Rev Solid State Mater Sci* **42**(4), 433-469 (2016).
- [79] L. Ćurković, R. Veseli, I. Gabelica, I. Žmak, I. Ropuš, et al., “A review of microwave-assisted sintering technique,” *Trans Famena* **45**(1), 256786 (2021).
- [80] A. W. Fliflet, R. W. Bruce, R. P. Fischer, D. Lewis, et al., “A study of millimeter-wave sintering of fine-grained alumina compacts,” *IEEE Trans Plasma Sci* **28**(3), 924-935 (2000).

- 
- [81] I. N. Sudiana, R. Ito, S. Inagaki, K. Kuwayama, K. Sako, et al., “Densification of alumina ceramics sintered by using sub-millimeter wave gyrotron,” *J Infra Milli Terahertz Waves* **34**, 627-638 (2013).
- [82] G. A. Kriegsmann, “Thermal runaway in microwave heated ceramics: A one-dimensional model,” *J Appl Phys* **71**(4), 1960 (1992).
- [83] M. S. Spatz, D. J. Skamser, and D. L. Johnson, “Thermal Stability of Ceramic Materials in Microwave Heating,” *J Am Ceram Soc* **78**(4), 1041-1048 (1995).
- [84] C. A. Vriezinger, S. Sanchez-Pedreno, and J. Grasman, “Thermal runaway in microwave heating: a mathematical analysis,” *Appl Math Model* **26**(11), 1029-1038 (2002).
- [85] R. R. Menezes, P. M. Souto, and R. H. G. A. Kiminami, *Microwave fast sintering of ceramic materials. Sintering of Ceramics – New Emerging Techniques*, (A. Lakshmanan Intech Open, London, England, 2012).
- [86] X. Cheng, C. Zhao, H. Wang, Y. Wang, and Z. Wang, “Mechanism of irregular crack-propagation in thermal controlled fracture of ceramics induced by microwave,” *Mech Ind* **21**(6), 610 (2020).
- [87] T. Garnault, D. Bouvard, J. M. Chaix, S. Marinel, and C. Harnois, “Is direct microwave heating well suited for sintering ceramics?” *Ceramics International* **47**(12), 16716-16729 (2021).



- [88] K. H. Brosnan, G. L. Messing, D. K. Agrawal, "Microwave sintering of alumina at 2.45 GHz," *J Am Ceram Soc* **86**(8), 1307-1312 (2003).
- [89] A. Chanda, S. Dasgupta, S. Bose, A. Bandyopadhyay, "A Microwave sintering of calcium phosphate ceramics," *Mater Sci Eng C* **29**(4), 1144-1149 (2009).
- [90] P. Figiel, M. Rozmus, B. Smuk, "Properties of alumina ceramics obtained by conventional and nonconventional methods for sintering ceramics," *J Achiev Mater Manuf Eng* **48**(1), 29-34 (2011).
- [91] J. Croquesela, D. Bouvard, J. Chaix, C. P. Carry, S. Saunier, et al. "Direct microwave sintering of pure alumina in a single mode cavity: Grain size and phase transformation effects," *Acta Mater* **116**, 53-62 (2016).
- [92] M. Shukla, S. Ghosh, N. Dandapat, A. K. Mandal, V. K. Balla, "Comparative study on conventional sintering with microwave sintering and vacuum sintering of Y<sub>2</sub>O<sub>3</sub>-Al<sub>2</sub>O<sub>3</sub>-ZrO<sub>2</sub> ceramics," *J Mater Sci Chem Eng* **42**(2), 71-78 (2016).
- [93] S. Ramesh, N. Zulkifli, C. Y. Tan, Y. H. Wong, F. Tarlochan, et al., "Comparison between microwave and conventional sintering on the properties and microstructural evolution of tetragonal zirconia," *Ceram Int* **44**(8): 8922-8927 (2018).





- [94] K. I. Rybakov, V. E. Semenov, "Possibility of plastic deformation of an ionic crystal due to the nonthermal influence of a high-frequency electric field," *Phys Rev B Condens Matter* **49**(1), 64-68 (1994).
- [95] S. A. Freeman, J. H. Booske, R. F. Cooper, "Microwave field enhancement of charge transport in sodium chloride," *Phys Rev Lett* **74**(11), 2042- 2045 (1995).
- [96] J. H. Booske, R. F. Cooper, S. A. Freeman, K. I. Rybakov, V. E. Semenov, "Microwave ponderomotive forces in solid-state ionic plasmas," *Phys Plasmas* **5**, 1664 (1998).
- [97] R. Wroe, A. T. Rowley, "Evidence for a non-thermal microwave effect in the sintering of partially stabilized zirconia," *J Materials Sci* **31**, 2019-2026 (1996).
- [98] A. Badev, R. Heuguet, S. Marinel, "Induced electromagnetic pressure during microwave sintering of ZnO in magnetic field," *J Eur Ceram Soc* **33**(6), 1185-1194 (2013).
- [99] Y. Xiao, F. Xu, B. Dong, W. Liu, X. Hu, "Discussion on the Local Magnetic Force between Reversely Magnetized Micro Metal Particles in the Microwave Sintering Process," *Metals* **7**(2), 47 (2017).
- [100] F. Xu, B. Dong, X. Hua, Y. Wang, W. Liu, et al., "Discussion on magnetic-induced polarization Ampere's force by in situ observing the special particle growth of alumina during microwave sintering," *Ceram Int* **42**(7), 8296-8302 (2016).



- [101] A. Birnboim, J. P. Calame, Y. Carmel, “Microfocusing and polarization effects in spherical neck ceramic microstructures during microwave processing,” *J Appl Phys* **85**, 478-482 (1999).
- [102] X. Qiao, X. Xie, “The effect of electric field intensification at interparticle contacts in microwave sintering,” *Sci Rep* **6**, 32163 (2016).
- [103] J. A. Menéndez, E. J. Juárez-Pérez, E. Ruisánchez, J. M. Bermúdez, A. Arenillas, “Ball lightning plasma and plasma arc formation during the microwave heating of carbons,” *Carbon* **49**(1), 346-349(2011).
- [104] M. Liu, L. Zhang, W. Zhou, J. Gao, P. Wang, et al., “The mechanism of microwave-induced discharge between submillimeter active coke,” *Plasma Sources Sci Technol* **29**(7), 075015 (2020).
- [105] S. Horikoshi, A. Osawa, S. Sakamoto, N. Serpone, “Control of microwave-generated hot spots. Part V. Mechanisms of hot-spot generation and aggregation of catalyst in a microwave-assisted reaction in toluene catalyzed by Pd-loaded AC particulates,” *Appl Catal A, General* **460-461**, 52-60 (2013).
- [106] Haneishi, S. Tsubaki, E. Abe, M. M. Maitani, E. Suzuki, et al., “Enhancement of fixed-bed flow reactions under microwave irradiation by local heating at the vicinal contact points of catalyst particles,” *Sci Rep* **9**, 222 (2019).



[107] E. Siegel, "Sparks fly when you microwave grapes: here's the science of why," *Big Think* (2021).

[108] Li-Chung Liu, Ming-Syun Lin and Kwo Ray Chu, "Microwave-Induced Attractive Force Between Dielectric Spheres-A Potential Non-Thermal Effect in Microwave Sintering," *Mod Concept Material Sci.* **4**(5) (2022).

[109] D. J. Griffiths, *Introduction to Electrodynamics*, 4th ed. (Pearson Education, Boston, 2013).

[110] A. A. Demkov, A. Navrotsky, *Materials Fundamentals of Gate Dielectric* (Springer, Dordrecht, Netherlands, 2005).

[111] S. X. Zhang, J. B. Li, H. Z. Zhai, J. H. Dai, "Low temperature sintering and dielectric properties of  $(\text{Zr}_{0.8}\text{Sn}_{0.2})\text{TiO}_4$  microwave ceramics using  $\text{La}_2\text{O}_3/\text{BaO}$  additives," *Mater Chem Phys* **77**(2), 470-475 (2002).

[112] A. Chang, J. Jian, "The orientation growth of grains in doped  $\text{BaTiO}_3$  PTCR materials by microwave sintering," *J Mater Proc Tech* **137**, 100-101 (2003).